

Structure and Seasonal Variability of the Arctic Boundary Current North of Severnaya Zemlya



Key Points:

- We quantify the Arctic Boundary Current (ABC) transport north of Severnaya Zemlya with a 2015–2018 mooring array
- Hydrographic changes along the ABC pathway are most prominent at the continental slope due to the interaction with shelf water
- Seasonality of water masses from the shelf sea was observed in transport, temperature and off-shelf excursions within the ABC







Correspondence to:

E. Ruiz-Castillo,
eruiocas@awi.de

Citation:

Ruiz-Castillo, E., Janout, M., Hölemann, J., Kanzow, T., Schulz, K., & Ivanov, V. (2023). Structure and seasonal variability of the Arctic Boundary Current north of Severnaya Zemlya. *Journal of Geophysical Research: Oceans*, 128, e2022JC018677. <https://doi.org/10.1029/2022JC018677>

Received 30 MAR 2022
 Accepted 27 DEC 2022

Eugenio Ruiz-Castillo¹ , Markus Janout¹ , Jens Hölemann¹ , Torsten Kanzow^{1,2} , Kirstin Schulz³ , and Vladimir Ivanov^{4,5} 

¹Alfred-Wegener-Institut, Helmholtz-Zentrum für Polar- und Meeresforschung, Bremerhaven, Germany, ²Department of Physics and Electrical Engineering, University of Bremen, Bremen, Germany, ³University of Texas, Oden Institute for Computational Engineering and Sciences, Austin, TX, USA, ⁴Lomonosov Moscow State University, Geography Faculty, Oceanology Department, Moscow, Russia, ⁵Arctic and Antarctic Research Institute, St. Petersburg, Russia

Abstract We assessed the spatial and temporal variability of the Arctic Boundary Current (ABC) using seven oceanographic moorings, deployed across the continental slope north of Severnaya Zemlya in 2015–2018. Transports and individual water masses were quantified based on temperature and salinity recorders and current profilers. Our results were compared with observations from the northeast Svalbard and the central Laptev Sea continental slopes to evaluate the hydrographic transformation along the ABC pathway. The highest velocities ($>0.30 \text{ m s}^{-1}$) of the ABC occurred at the upper continental slope and decreased offshore to below 0.03 m s^{-1} in the deep basin. The ABC showed seasonal variability with velocities two times higher in winter than in summer. Compared to upstream conditions in Svalbard, water mass distribution changed significantly within 20 km of the shelf edge due to mixing with- and intrusion of shelf waters. The ABC transported $4.15 \pm 0.3 \text{ Sv}$ in the depth range 50–1,000 m, where 0.88 ± 0.1 , 1.5 ± 0.2 , 0.61 ± 0.1 and $1.0 \pm 0.15 \text{ Sv}$ corresponded to Atlantic Water (AW), Dense Atlantic Water (DAW), Barents Sea Branch Water (BSBW) and Transformed Atlantic Water (TAW). 62–70% of transport was constrained to within 30–40 km of the shelf edge, and beyond 84 km, transport increases were estimated to be 0.54 Sv. Seasonality of TAW derived from local shelf-processes and advection of seasonal-variable Fram Strait waters, while BSBW transport variability was dominated by temperature changes with maximum transport coinciding with minimum temperatures. Further Barents Sea warming will likely reduce TAW and BSBW transport leading to warmer conditions along the ABC pathway.

Plain Language Summary We assessed the structure and seasonal variability of the flow and water masses of the Arctic Boundary Current (ABC) in the region north of Severnaya Zemlya. This current is important in the Arctic Ocean as it transports relatively warm and saline waters along the Eurasian Arctic continental slope. We quantified the flow, transport and hydrographic variability of the ABC. Compared to observations from upstream, our results indicate that the water masses away from the shelf break maintained the hydrographic characteristics from upstream. In contrast, the water masses near the shelf break were significantly cooled and freshened due to intrusion of- and mixing with shelf waters. The water masses near the shelf break showed a seasonal signal in volume transport and temperature which derives from local shelf processes, advection of seasonal-variable waters along the ABC pathway and the seasonal cooling of the Barents Sea. If the warming trend in the Barents Sea continues, warmer waters are expected to be advected eastward along the Eurasian continental slope by the ABC.

1. Introduction

Warm and saline waters from the North Atlantic enter the Arctic Ocean through Fram Strait and the western Barents Sea (Aagard et al., 1987; Schauer et al., 2004) (Figure 1a) and propagate cyclonically along the Arctic continental slope with the Arctic Boundary Current (ABC). These water masses are significantly cooled during the along-slope passage (Bluhm et al., 2020) due to a variety of processes such as vertical heat transfer (Ivanov et al., 2009; Polyakov et al., 2010), heat exchange with the atmosphere and sea ice (Duarte et al., 2020; Ivanov et al., 2016; Rudels et al., 1996, 2005) or heat loss within the bottom boundary layer (Schulz et al., 2021). In the Barents Sea, waters from the North Atlantic are transformed into Barents Sea Branch Water (BSBW) (Gammelsrød et al., 2009; Schauer et al., 2002). The waters cool and freshen due to vertical mixing with cold and less saline shelf waters (Lind et al., 2016, 2018) and air-sea heat loss (Schauer et al., 2002). BSBW then enters the Arctic Ocean via St. Anna Trough as a density current (Årthun et al., 2011; Schauer et al., 1997, 2002; Shapiro

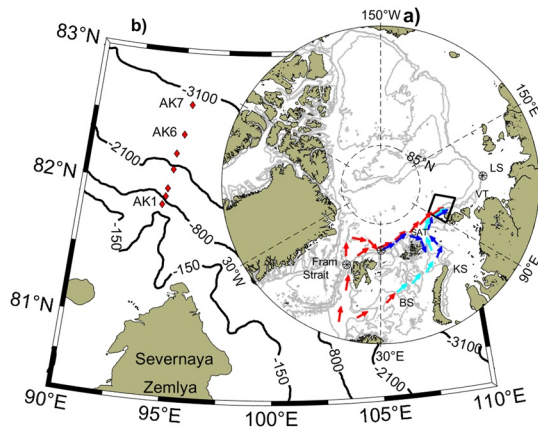


Figure 1. Maps of (a) the Arctic Ocean and (b) the study area. In (a) the black circle and asterisk indicate the location of the time series in the West Spitsbergen current region and previous observations in northeast Svalbard and in the central Laptev Sea. In (a) a schematic of the circulation is shown where waters from the Atlantic Ocean (Dense Atlantic Water and Atlantic Water), Barents Sea Branch Water and Transformed Atlantic Water are represented by red, light blue and dark blue arrows, respectively. BS, KS, LS, VT, and SAT stand for Barents Sea, Kara Sea, Laptev Sea, Vilkitsky Trough and St. Anna Trough, respectively. Gray contours represent the 265, 400, and 2,500 m isobaths. In (b) red diamonds indicate the location of the moorings.

et al., 2003), and then joins the ABC along with waters from Fram Strait. Confluence of these waters sets up a cross-slope density gradient which leads to geostrophic adjustment (Pnyushkov et al., 2015). Consequently, both BSBW and waters from Fram Strait flow eastward along the ABC pathway.

The ABC further cools between St. Anna Trough and the Laptev Sea (Pnyushkov et al., 2015; Rudels et al., 2000; Schulz et al., 2021). This region generally features Arctic conditions with near-freezing surface waters separated from the warm Atlantic layer by a strong halocline (Fer, 2009; Rudels, 2009; Rudels et al., 1996). However, within the last decade, observations highlight a transition toward ocean characteristics that are commonly found closer to the Atlantic inflow. These include increases in sub-surface temperatures along with a decrease in sub-surface stratification (Polyakov et al., 2013, 2017). This process is referred to as Atlantification and described to contribute to decreasing the sea-ice thickness and concentration in the Nansen Basin (Asbjørnsen et al., 2020; Carmack et al., 2015; Ivanov et al., 2012). Upward heat loss from the ABC plays a major role in Atlantification (Ivanov et al., 2018; Polyakov et al., 2013, 2017, 2020), particularly in winter when vertical heat fluxes are greater (Ivanov et al., 2018; Polyakov et al., 2013). In summer vertical heat fluxes were estimated to represent less than 20% of the observed ABC cooling (Schulz et al., 2021). Nonetheless, cooling of the ABC has been suggested to mainly result from mixing with cold shelf waters (Janout et al., 2017; Lenn et al., 2009; Rudels et al., 2000; Schulz et al., 2021; Woodgate et al., 2001), which are supplied continuously into the Arctic Ocean (Årthun et al., 2011; Shapiro et al., 2003). However,

the temporal and spatial effects of the shelf waters exports on the hydrography of the ABC remain unclear. It is crucial to understand the relevant cooling processes along the ABC pathway. For instance, reductions in the rate of wintertime cooling of shelf water in the Barents Sea may lead to advection of warmer waters into the Arctic Ocean and the eastern Arctic continental slopes. Most of our understanding is based on model studies and few synoptic observations that are constrained mainly to small areas and ice-free periods. These studies, however, cannot provide temporal assessments of the transformation of water masses or intrusion of shelf waters along the ABC pathway. In contrast, long-term (1–2 years) mooring-based analyses of water mass variability and transport along the Eurasian Arctic continental slope have been carried out in few selected regions such as northeast of Svalbard (Pérez-Hernández et al., 2019) and the Laptev Sea (Baumann et al., 2018). However, the >2,000 km distance between these sites hinders a detailed analysis of the processes cooling the water masses along the ABC pathway.

Our study focuses on the along-slope transport north of Severnaya Zemlya (Figure 1b). This dynamic region is characterized by the convergence of waters from Fram Strait and the Barents Sea, with the latter entering the Arctic Ocean through St. Anna Trough only 400–600 km upstream of our focus region. Based on an array of seven moorings deployed from the shelf break across the continental slope into the basin between 2015 and 2018, we analyze the ABC's structure and seasonality and assess the hydrographic properties and water mass transports entering the eastern Arctic continental slope region. We contrast our results with long-term records from Fram Strait and the central Laptev Sea to discuss the water mass transformation along the ABC pathway.

2. Methods

2.1. Current and Hydrographic Time Series

A high-resolution mooring array was used to analyze the water masses, transports and structure of the ABC north of Severnaya Zemlya (Figure 1b). The array consisted of 7 moorings (AK1–AK7) arranged over an 84 km-wide stretch across the continental slope from August 2015 to September 2018 in water depths between 300 m (AK1) and 3,000 m (AK7) (Figure 2). Overall, the array was under sea ice between November and June–July while in the period June–November more ice-free conditions were found. In the upper continental slope (AK1–AK3) the Rossby radius of deformation was estimated to be ~5 km in accordance with previous studies (Nurser & Bacon, 2014). The distance between moorings was on average 6.5 km, which is greater, but comparable to the local Rossby radius. Between moorings AK3 and AK7 the distance between moorings increases to an average of ~18 km with standard deviation of ± 4.6 km, a length scale that is also greater but comparable to the Rossby

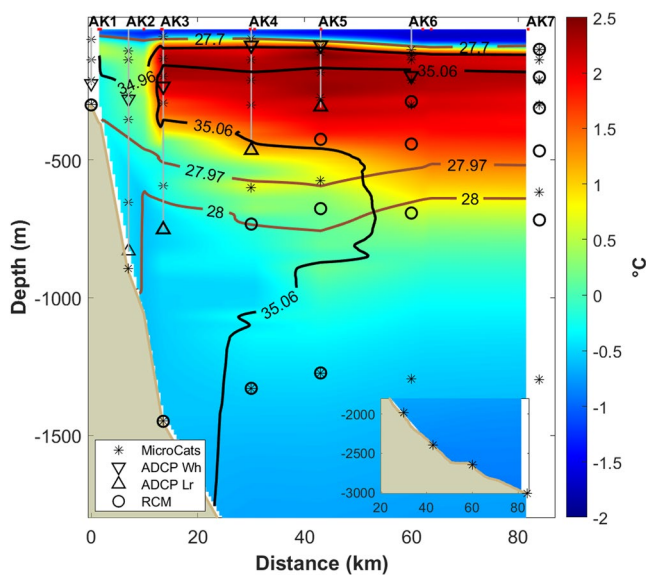


Figure 2. The color shading shows the cross-slope section of temperature obtained from Conductivity, Temperature, and Depth casts (red dots) during recovery of moorings in August 2018. The distributions of salinity and density are denoted by the black and brown contours, respectively. Superimposed is the diagram of the mooring array deployed for 3 years between 2015 and 2018. The black asterisks indicate the location of temperature and salinity time sensors (SBE microcats), triangles represent the Acoustic Current Doppler Profilers (ADCP's) (RDI workhorse and longranger) and black circles the location of rotor current meters (RCM). Gray points show the depth range of the velocities obtained from ADCP's. The small figure shows the location of the instruments below 1,800 m.

radius of deformation which in this region has been estimated to be of order 10 km (Nurser & Bacon, 2014). The mooring array was equipped with Acoustic Current Doppler Profilers (ADCP's, Teledyne RDI), rotor current meters (RCM) and CTD (Conductivity, Temperature, and Depth) sensors (SeaBird Microcats). The sampling intervals were different depending on the sensor from 30 to 60 min for temperature and salinity recorder, up to 90 min for ADCP's and 120 min for single point Aanderaa current meters. The vertical bin size of the ADCP's ranged from 2 m for 300 KHz Workhorse to 8 m bins for 75 KHz Longranger ADCP's. Different parameters were investigated for quality control, and data points that did not pass specified thresholds (beam correlations >64%, error velocity <10 cm s⁻¹, percent-of-good >50%, pitch/roll <20°) were discarded. Velocities from ADCP and RCM were corrected for magnetic field (~50°) and error compasses. Time series of temperature and salinity were processed using automated seabird routines and calibrated with hydrographic data from CTD casts obtained during the mooring's recovery. More details on instrument depths and sampling period are provided in Table 1. The analysis was complemented with hydrographic time series from September 2016 to July 2018 from Fram Strait in the West Spitsbergen Current region (Figure 1a) (Von Appen et al., 2019). To remove fluctuations such as tides, high frequencies were removed from all time series with a running average window of 14 days. With this 14-day filter, most eddies would have been eliminated as well. The data sets were subsequently subsampled at a temporal resolution of 1 day. Gaps in the salinity records were removed by using a distance-weighted average interpolation. Near the bottom at AK1 and AK2, events of density inversion, produced by the sensor accuracies, were observed. These events accounted for 45% and 33% of the observations, respectively. In these periods the absolute average density difference was 0.0063 kg m⁻³ with a maximum of 0.02 kg m⁻³ for AK1, while for AK2 maximum differences were below 0.008 kg m⁻³. Nonetheless differences in temperature indicated the water column was not mixed at these depths. During these events density

was assumed to be homogeneous between the two bottom time series and bottom salinity was recalculated from temperature and density. Conservative Temperature, Absolute Salinity and potential density were calculated using the Thermodynamic equation of state (McDougall & Barker, 2011). Similar to the hydrographic measurements, gaps in the current meter records (Table 1) were vertically interpolated based on velocity data from adjacent depths using a distance-weighted average interpolation. For gaps in the deepest time series, the existing velocities were scaled with adjacent depths and missing velocities were assumed to be represented by the scaled velocities of the adjacent depths. In this study we focused on the velocity component perpendicular to the mooring section, thus the horizontal velocities were rotated (36°) accordingly into along-slope (*u*) and cross-slope directions (*v*). Velocities in the water column were used to assess the main modes of variability of the flow in the along-slope direction through an Empirical Orthogonal Function analysis. To identify the regions where most of the variability of the ABC flow occurred, we computed the Eddy Kinetic energy (EKE). To remove tidal fluctuations a running average with a 2-day window was performed on the original velocity data from ADCP's and RCM's. The corresponding velocities (*u_a* and *v_a*) were used to calculate EKE in the form:

$$EKE = \frac{1}{2} \langle u_a'^2 + v_a'^2 \rangle \quad (1)$$

where (*u_a'*, *v_a'*) = (*u_a* - <*u_a*>, *v_a* - <*v_a*>) with <> and ' representing the temporal mean and deviations from the temporal mean, respectively. To rule out seasonal contributions, EKE was calculated over periods of 30 days.

2.2. Water Mass Classification

The water mass classification (Table 2) utilized here was based on the transformation of waters from the Atlantic Ocean in the Barents Sea and along the ABC pathway from the West Spitsbergen Current region to Severnaya Zemlya (Figure 1a). The water column was divided into surface, intermediate and deep density layers following Rudels et al. (2005) and Rudels (2009). The surface and deep density layers were characterized by densities lower

Table 1

Positions, Water Depth Range and Time Periods of the Hydrographic and Velocity Instruments of the Moorings at Severnaya Zemlya (AK) and Fram Strait (F4)

| Id | Position | Depths of temperature and salinity time series (m) | | Depth-range of velocity measurements (m) | |
|-----|-----------|--|----------------------------------|--|------------------------------------|
| | | | Period | | Period |
| AK1 | 94.3422 E | 63, 135, 210, 299 | 29 August 2015–25 August 2018 | ADCP: 22-222 | 28 August 2015–25 August 2018 |
| | 81.8448 N | | | RCM: 300 | 28 August 2015–13 February 2018 |
| AK2 | 94.482 E | 103, 135, 263, 353, 653,895 | 29 August 2015–25 August 2018 | ADCP: 28-280 | 25 August 2015–29 August 2018 |
| | 81.9028 N | | | ADCP: 279-831 | 25 August 2015–29 August 2018 |
| AK3 | 94.5433 E | 50, 131, 196, 293, 593, 1,448 | 29 August 2015–23 August 2018 | ADCP: 24-232 | 23 August 2015–29 August 2018 |
| | 81.9622 N | | | ADCP: 233-753 | 23 August 2015–29 August 2018 |
| AK4 | 94.7723 E | 60, 135, 210, 300, 600, 1,330, 1,980 | 31 August 2015–22 August 2018 | ADCP: 41–465 | 30 August 2015–22 August 2018 |
| | 82.1047 N | | | ADCP: 6-48 | 30 August 2015–22 August 2018 |
| AK5 | 94.8462 E | 87,108, 183, 273, 575, 1,274, 2394 | 24 September 2015–24 August 2018 | ADCP: 35-307 | 23 September 2015–24 August 2018 |
| | 82.2243 N | | | ADCP: 9-83 | 23 September 2015–26 June 2018 |
| AK6 | 95.2177 E | 98, 121, 135, 210, 300, 1,295, 2646 | 30 September 2015–20 August 2018 | ADCP: 14-96 | 24 September 201–22 August 2018 |
| | 82.3672 N | | | RCM: 288 | 24 September 2015–7 August 2018 |
| AK7 | 95.5 E | 99, 135, 210, 300, 618, 1,298, 3,015 | 30 September 2015–20 August 2018 | RCM: 442 | 24 September 2015–23 December 2017 |
| | 82.5858 N | | | RCM: 693 | 24 September 2015–23 December 2017 |
| AK7 | 95.5 E | 99, 135, 210, 300, 618, 1,298, 3,015 | 30 September 2015–20 August 2018 | RCM: 98 | 24 September 2015–21 December 2017 |
| | 82.5858 N | | | RCM: 199 | 24 September 2015–10 February 2017 |
| AK7 | 95.5 E | 99, 135, 210, 300, 618, 1,298, 3,015 | 30 September 2015–20 August 2018 | RCM: 311 | 24 September 2015–10 December 2017 |
| | 82.5858 N | | | RCM: 467 | 24 September 2015–15 January 2016 |
| AK7 | 95.5 E | 99, 135, 210, 300, 618, 1,298, 3,015 | 30 September 2015–20 August 2018 | RCM: 718 | 24 September 2015–22 August 2018 |
| | 82.5858 N | | | RCM: 718 | 24 September 2015–22 August 2018 |

Table 1
Continued

| Id | Position | Depths of temperature and salinity time series (m) | | Depth-range of velocity measurements (m) | |
|----|-----------------------|--|--|--|--|
| | | Period | | Period | |
| F4 | 7.0005 E 79.0002 N | 68, 171, 263, 394, 507, 735, 1,172 | | 29 July 2016–15 July 2018 | |

and greater than 27.70 and 27.97 kg m⁻³, respectively, thus the intermediate density layer was bounded by the 27.97 and 27.7 kg m⁻³ isopycnals. Waters from the North Atlantic (AW and DAW) in the West Spitsbergen Current in Fram Strait are characterized by salinities above 35.06 g kg⁻¹ (Figure 3a). Based on their density range, in the intermediate and deep density layers the waters from the North Atlantic were divided into Atlantic Water (AW) and Dense Atlantic Water (DAW) (Rudels, 2009). These waters with unmodified characteristics from Fram Strait were observed in the eastern Arctic north of the Severnaya Zemlya continental slope (Figures 3b and 3c). The Arctic Water (ArW) chiefly occupies the surface density layer (Baumann et al., 2018; Rudels et al., 2000). However, the 3-year hydrographic record utilized in this study enabled us to identify events of Arctic surface water within the intermediate density layer at 50 and 60 m depth (not shown). Low temperatures ($T < -1.5^{\circ}\text{C}$) indicate a surface origin and increases in salinity suggest brine rejection associated with sea-ice formation (Baumann et al., 2018; Ivanov et al., 2016; Polyakov et al., 2013; Rudels et al., 2005). Therefore, water occurring in the surface density layer and within the intermediate layer below -1.5°C was termed Arctic Water (ArW). Throughout the record different hydrographic characteristics between the shallowest and the following time series (~ 130 m) were observed. Thus, in this time-period between 2015 and 2018 the mixed layer seemed to be constrained above 130 m depth. The water with hydrographic properties found at the transition between Arctic Water and unmodified Atlantic Water (compared to properties upstream in Fram Strait) are referred to as Transformed Atlantic Water (TAW) (Table 2). The North Atlantic Water entering the Arctic Ocean through Barents Sea and St. Anna Trough, termed Barents Sea Branch Water (BSBW), was denser than water in the intermediate density layer and less saline than DAW from Fram Strait. Finally, in the temperature-salinity diagram (Figures 3b and 3c) BSBW is located within the deep density layer and characterized by salinities below 35.06 g kg⁻¹ (Arthun et al., 2011; Dmitrenko et al., 2009; Rudels et al., 2004; Schauer et al., 2002).

2.3. Estimation of Water Mass Transport, Mean Velocity, Conservative Temperature and Absolute Salinity

The moorings were primarily designed to observe the Atlantic Water circulation. Most of the sensors were installed between 50 and 700 m depth where most of the hydrographic changes occur (Figure 2). Below 700 m hydrographic changes were relatively small (Figure 2). At each mooring site, vertical profiles were interpolated every 20 m down to $\sim 1,500$ m by use of distance-weighted average interpolation. Consequently, every 40 m depth, velocity and hydrographic measurements were horizontally interpolated every 8 and 5 km, respectively. To quantify transports for each water mass, we produced gridded cross-slope sections of Absolute Salinity (S_i), Conservative Temperature (T_i) and along-slope velocity (u_i) using optimal interpolation (Jerónimo & Gómez-Valdés, 2007; Le Traon, 1990). Sections were constrained by the local topography. However, available bathymetry data mismatched with the depths of the moorings near the shelf edge (AK1 and AK2). Furthermore, during instrument deployment, bottom depth recordings were not possible due to

Table 2

Water Masses Definition and Mean and Standard Error of Salinity, Mean Velocity-Weighted Temperature, Velocity and Transport for Each Water Mass

| Water mass | Ranges | Mean salinity (g kg ⁻¹) | Mean velocity-weighted temperature (°C) | Mean velocity (m s ⁻¹) | Mean transport (Sv) |
|----------------------------------|--|-------------------------------------|---|------------------------------------|---------------------|
| Transformed Atlantic Water (TAW) | $27.7 < \sigma_0 < 27.97$ CT $> -1.5^{\circ}\text{C}$ $S < 35.06$ g kg ⁻¹ | 34.97 ± 0.006 | 0.8 ± 0.2 | 0.09 ± 0.009 | 1.0 ± 0.15 |
| Atlantic Water (AW) | $27.7 < \sigma_0 < 27.97$ $S > 35.06$ g kg ⁻¹ | 35.1 ± 0.002 | 1.9 ± 0.03 | 0.04 ± 0.004 | 0.88 ± 0.11 |
| Dense Atlantic Water (DAW) | $27.97 < \sigma_0 < S > 35.06$ g kg ⁻¹ | 35.1 ± 0.003 | 0.64 ± 0.03 | 0.04 ± 0.004 | 1.5 ± 0.19 |
| Barents Sea Branch Water (BSBW) | $27.97 < \sigma_0 < S < 35.06$ g kg ⁻¹ | 35.04 ± 0.003 | 0.26 ± 0.09 | 0.14 ± 0.017 | 0.61 ± 0.10 |
| Arctic Water (ArW) | $27.7 > \sigma_0; 27.7 < \sigma_0 < 27.97$ CT $< -1.5^{\circ}\text{C}$ | na | na | na | na |

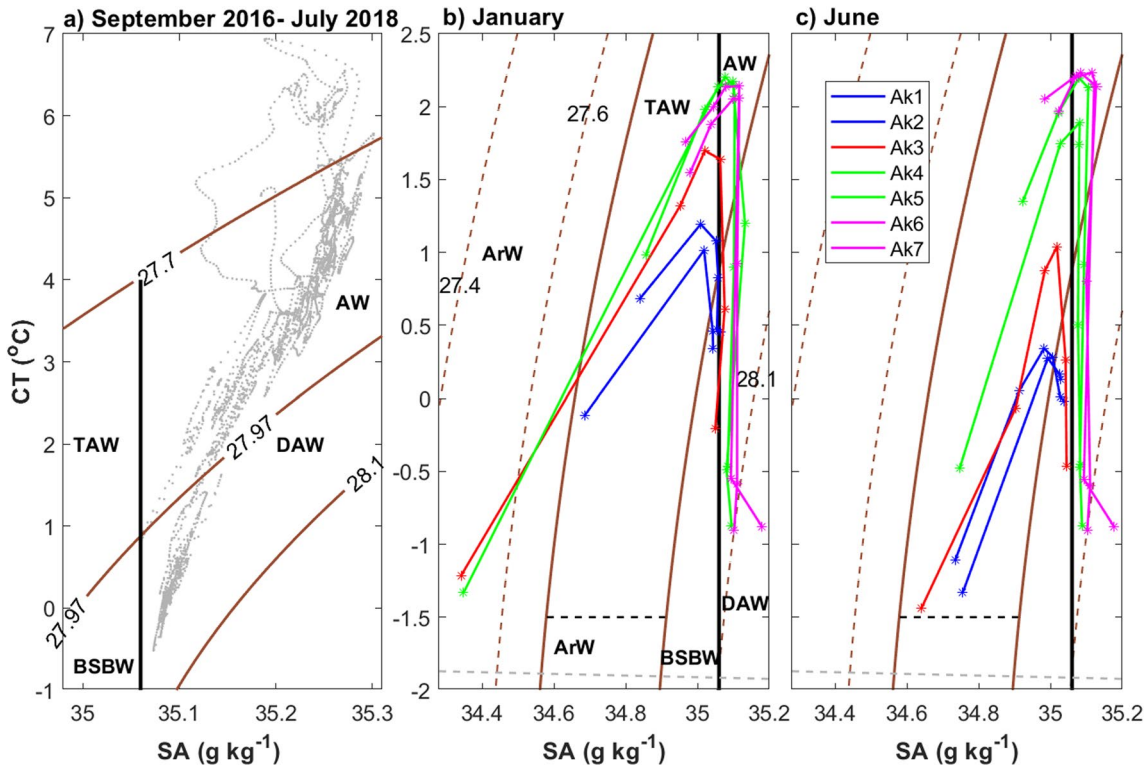


Figure 3. T-S diagrams from (a) Fram Strait for the period September 2016–July 2018 between 50 and 1,170 m depth at 79°N and 7°E and, (b) and (c) Severnaya Zemlya for January and June. In (b) and (c) solid brown contours represent the 27.7 and 27.97 kg m⁻³ isopycnals. Gray dashed line indicate the freezing point and the solid and dashed black lines represent the 35.06 g kg⁻¹ salinity and -1.5°C temperature, respectively. ArW, TAW, AW, BSBW, and DAW stand for Arctic Water, Transformed Atlantic Water, Atlantic Water, Barents Sea Branch Water and Dense Atlantic Water, respectively.

difficult sea-ice conditions. Therefore, in the upper continental slope region we created a bathymetric chart along the mooring array from the CTD casts carried out during the mooring recovery between August and September 2018. For the deep basin region, we merged our bathymetric chart with bathymetric data sets from IBCAO (Jakobsson et al., 2020). At each time step hydrographic and velocity data points were interpolated onto a regular grid with horizontal and vertical resolution of 1 km and 1 m so that each grid point represents 1,000 m². Horizontal and vertical correlation scales were 15 km and 115 m, respectively. For the whole record the interpolation error for hydrographic parameters was estimated to be lower than 6% for the whole section, while for velocity the error was below 10% in the upper 700 m. Below this depth, the interpolated along-slope velocities (u_i) at 695 m were used to represent the area down to 1,000 m where the flow was considered depth-independent, which is consistent with the velocity records. The density was computed from the gridded mooring-based Conservative Temperature (T_i) and Absolute Salinity (S_i) sections. The grids with the hydrographic characteristics defined in Table 2 were localized. For each water mass we estimated the daily area covered (A) and mean velocity (\bar{u}_i), along with the transport-weighted temperature (T_w) which was calculated according to:

$$T_w = \int_{sl}^{nl} \int_{ll}^{ul} u_i T_i dy dz / \int_{sl}^{nl} \int_{ll}^{ul} u_i dy dz \quad (2)$$

where sl , nl , ll , and ul stand for the southern, northern, lower and upper limits of each water mass. Transports (U) were computed individually from area (A) and mean velocity (\bar{u}_i) in the form:

$$U(t) = A(t)\bar{u}_i(t) \quad (3)$$

We assessed the uncertainty of the interpolation method and the uncertainty related to the measurements by adding random noise, in the range ± 2 cm s⁻¹, to the velocity records in three iterations. Consequently, we

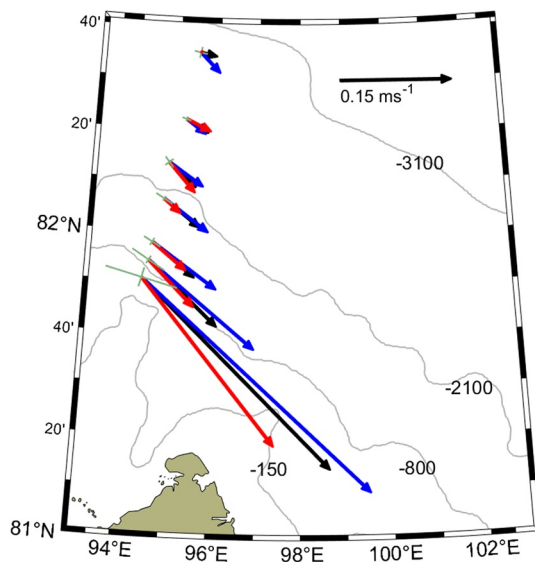


Figure 4. The map shows the 190–200 m velocity averaged over the whole record (black), January (blue) and June (red). Gray contours represent the 150, 800, 2,100, and 3,100 m depth. At each mooring site the major and minor axes of the standard error ellipses are represented by the green lines.

estimated the daily mean velocity and transport for each water mass and together with the noise-free time series calculated the time-varying standard error. In the 3-year record, the maximum standard error of velocity for each water mass was below 0.5 cm s^{-1} while the maximum standard error of transport was 0.03, 0.05, 0.13, and 0.03 Sv for BSBW, AW, DAW, and TAW, respectively. To assess the relative influence of velocity (\bar{u}_i) and area (A) on transport, a transport decomposition was performed as follows:

$$U(t) = \langle A(t) \rangle \langle \bar{u}_i(t) \rangle + \langle A(t) \rangle \bar{u}_i(t)' + \bar{u}_i(t) \langle A(t)' \rangle + \bar{u}_i(t)' A(t)' \quad (4)$$

where the second and third terms on the right-hand side of Equation 4 are the contribution of the variations of velocity and area, respectively. The fourth term represents the contribution of the product of the deviations of velocity and area. A seasonal analysis of velocity, area, transport and temperature for each water mass was carried out. From the 3-year record the properties that fell within bimonthly periods (15 days) of a Julian year were averaged and the standard error was calculated. Throughout the study the different time-series were compared through a Pearson Correlation analysis with correlation coefficients (γ) significant at a p-value below 0.05, unless otherwise stated. Finally, Arctic Waters occurred in the upper part of the water column where sampling was incomplete and were thus excluded from further analyses as no robust transport assessment could be performed.

3. Results

3.1. The ABC Velocity Structure: Mean State and Variability

The flow in the continental slope region north of Severnaya Zemlya is dominated by the ABC, with a major along-shelf flow direction (Figure 4). Away from the slope in the Nansen Basin, the currents are also directed eastward though comparatively sluggish. The velocities decreased 64% within 8 km from 0.36 m s^{-1} at AK1 to 0.13 m s^{-1} at AK2 and further weakened to 0.07 m s^{-1} at AK3 (Figure 4). The observations indicate a baroclinic flow structure on the upper continental slope (Figure 5a). The velocities were highest ($>0.3 \text{ m s}^{-1}$) between 100 and 250 m depth at the 300 m isobath. Within 15 km of the shelf break, velocities remained above 0.1 m s^{-1} , while the velocities further off-shelf gradually decreased to below 0.025 m s^{-1} at AK6 and AK7 (Figures 4 and 5a). North of AK2 the velocities were nearly homogenous throughout the water column and indicate a barotropic flow structure. The regions with the highest velocities showed the greatest EKE with values above $21 \text{ cm}^2 \text{ s}^{-2}$ (Figure 5b). Averaged velocities and EKE were highly correlated ($\gamma = 0.82$). In the deep basin, EKE reduced to values below $7 \text{ cm}^2 \text{ s}^{-2}$. Consistently with the average velocities, the first spatial mode of variability, which accounts for 55% of the along-shelf flow variability (Figure 6a), indicates flow fluctuations to decay rapidly away from the coast with amplitudes at AK4 reaching less than 10% of those at AK1. Since the mode does not cross zero anywhere, it can be interpreted to represent a coherent, pulse-like motions of the ABC. The corresponding principal component (PC1) shows both seasonal and intra-seasonal variability at comparable amplitudes (Figures 6b and 6c). By applying a low- and pass-band Lanczos filter on the PC1, a comparison between the standard deviations indicate that the seasonal part of PC1 is 1.4-times greater than the intra-seasonal part. The second EOF mode represents 25% of the total variability and again shows a reduction in amplitude with increasing distance from the shelf-edge (Figure 6a). However, the flow reverses between AK1 and the offshore sites. This pattern represents a compensation between near-shore and offshore flows and is associated with strong horizontal shear between Ak1 and AK2, significantly stronger than the one diagnosed by mode 1. Interestingly, PC2 contains almost entirely seasonal variability (as opposed to intra-seasonal) with maximum positive values between July and January (Figures 6b and 6c).

The winter period from October to February was characterized by the highest ABC velocities. In January, the strongest velocities were observed above the upper continental slope (AK1-3) with values of 0.42, 0.19, and

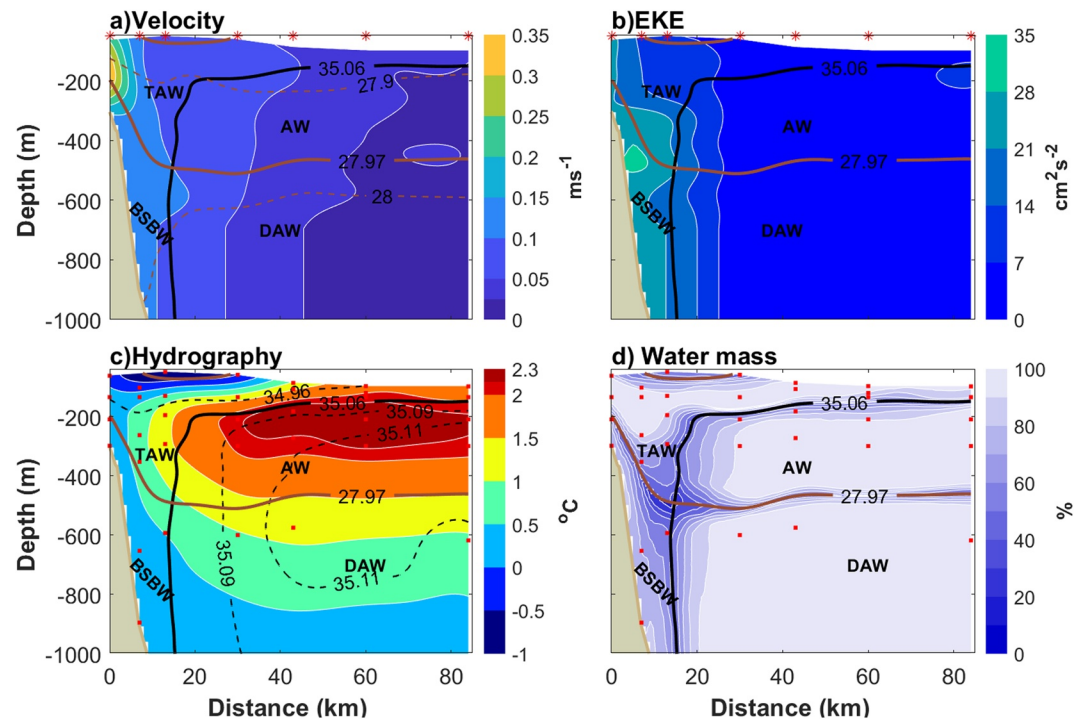


Figure 5. Cross-slope sections of mean (a) velocity, (b) Eddy Kinetic energy, (c) Conservative Temperature, and (d) temporal occurrence of each water mass. Thick brown and black contours represent the 27.7 and 27.97 kg m^{-3} isopycnals and the 35.06 g kg^{-1} isohaline, respectively. Brown and black dashed lines represent isopycnals and isohalines, respectively. Thick contours separate the different water masses. In (a) and (b) red asterisks indicate the location of the moorings. In (c) and (d) red dots represent the location of the hydrographic time series.

0.11 m s^{-1} (Figure 4). In the deep basin, the velocities gradually decreased to 0.04 m s^{-1} at AK6 and AK7 (Figure 4) and were nearly homogenous throughout the water column up to 60 km (Figure 7a). In contrast, on the upper continental slope, the intensity of the velocities varied throughout the water column. At the 300 m-isobath, maximum velocities ($>0.40 \text{ m s}^{-1}$) occurred at mid-depths between 100 and 220 m, while along the continental slope velocities greater than 0.2 m s^{-1} occupied the region between 50 and 500 m. Throughout the record, the weakest velocities occurred in April-June (Figure 7b). In June average velocities (0.08 m s^{-1}) accounted for ~61% of the intensity observed in January (0.13 m s^{-1}). Mean velocities at AK1, AK2, and AK3 were 0.29, 0.09, and 0.06 m s^{-1} and between AK6 and AK7 were below 0.025 m s^{-1} (Figure 4). The strongest velocities above 0.1 m s^{-1} occurred above 300 m in the vicinity of the 300 m isobath with maximum flow above 0.25 m s^{-1} at mid-depths (Figure 7b).

3.2. Mean Hydrography and Water Mass Variability in the ABC

The average spatial distribution of the water masses north of Severnaya Zemlya is shown in Figure 5c. Within the intermediate density layer, AW occupied the area 20 km away from the shelf break between ~180 and 500 m with maximum temperatures occurring above 350 m. TAW was found further from the shelf break above the AW as well as between the AW and the shelf break at 100–450 m. In the deep density layer ($\sigma_0 > 27.97 \text{ kg m}^{-3}$), the bottom part of the continental shelf and the region above the continental slope up to 18 km distance was occupied by BSBW. Off-shelf, DAW governed the region below AW. For the waters from the North Atlantic (DAW and AW) the maximum salinity ($>35.11 \text{ g kg}^{-1}$) was observed between 200 and 700 m depth (Figure 5c). BSBW and TAW were in the region where the EKE was the highest. The temporal occurrence of each water mass is shown in Figure 5d. DAW and AW were always located further from 20 km and showed small vertical fluctuations in the area covered by these water masses. TAW occurred mainly in the region above AW and down to 300 m and at a 10 km distance from the 300 m isobath. Below 300 m depth, the temporal occurrence dropped to 50%–60% which resulted from lateral intrusions of AW. The temporal occurrence of

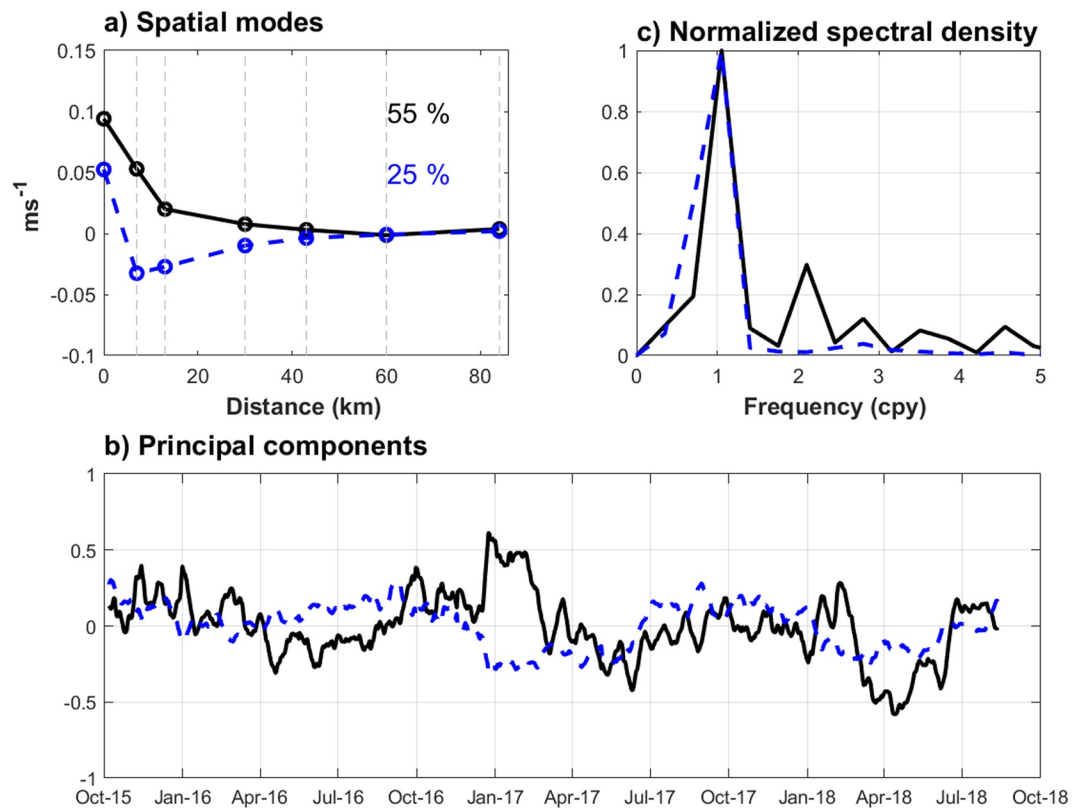


Figure 6. First (black) and second (blue) (a) depth-averaged spatial modes and (b) principal components of an empirical orthogonal function analysis. (c) Normalized spectral density of the principal components. The first and second modes account for 55% and 25% of the variability.

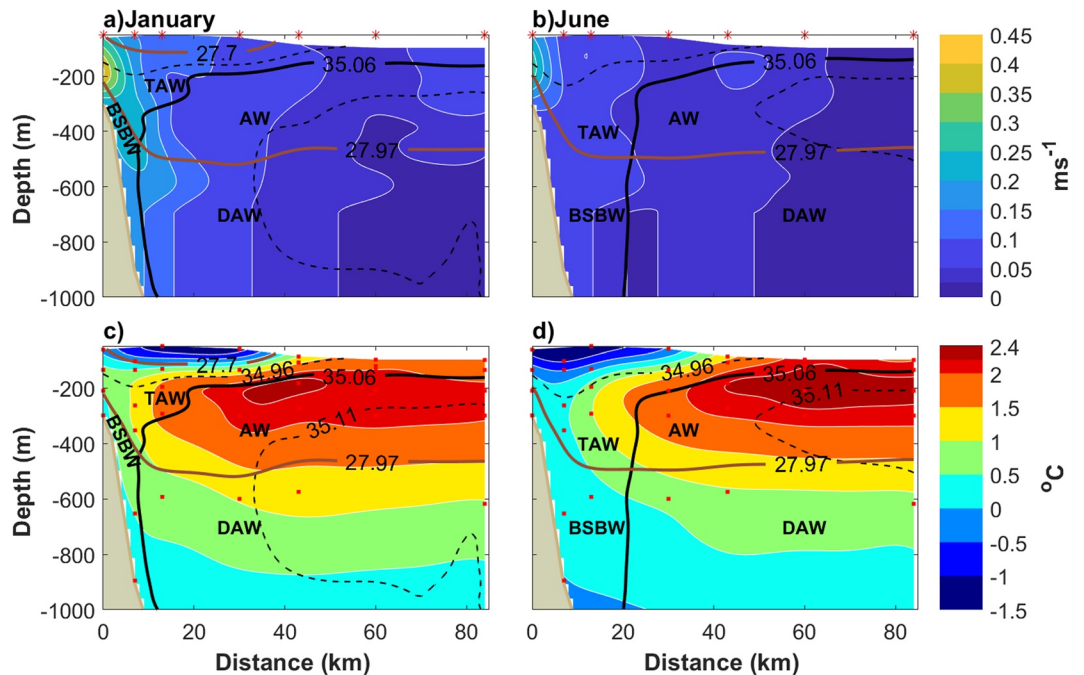


Figure 7. Cross-slope sections of mean velocity for (a) January and (b) June and mean Conservative Temperature for (c) January and (d) June. In (a) and (b) red asterisks indicate the location of the moorings and in (c) and (d) red dots represent the location of the hydrographic time series. Thick density and salinity contours separate the different water masses.

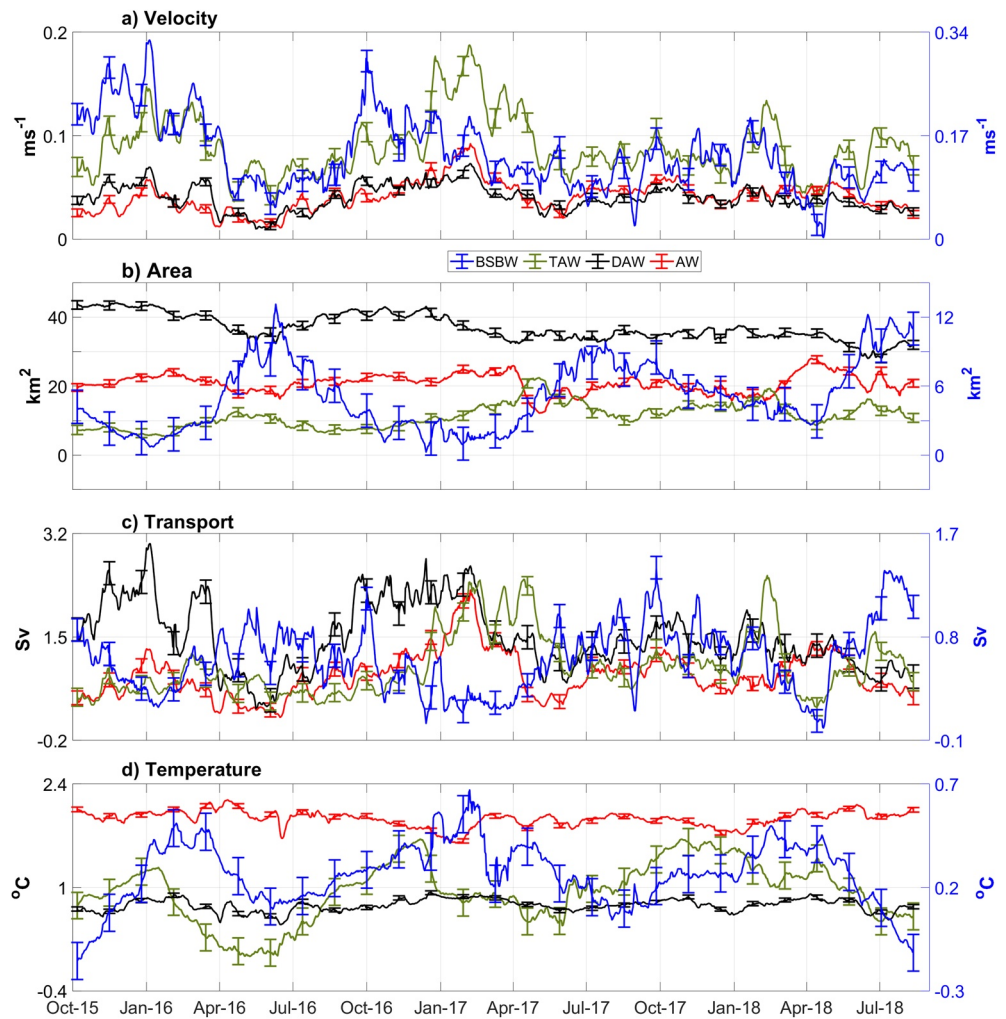


Figure 8. Time series of (a) velocity, (b) area, (c) transport and (d) velocity-weighted temperature for each water mass. In (a)-(d) the right axis corresponds to Barents Sea Branch Water (BSBW). Error bars indicate the standard error.

BSBW indicates the area this water mass covered fluctuated along the shelf break between 200 and 1,000 m depth. At 18 km, the relatively low temporal occurrence between BSBW and DAW indicates lateral displacement of these water masses.

Compared to the other water masses, BSBW showed the largest average velocity of $0.14 \pm 0.017 \text{ m s}^{-1}$ followed by TAW ($0.09 \pm 0.009 \text{ m s}^{-1}$) (Figure 8a, Table 2). These water masses were distributed near the shelf edge where the ABC is strongest (Figures 4–6). In the period October 2015 to May 2017, the velocity of BSBW showed maximums and minimums occurring in October–April and May–September, respectively. For TAW, the most intense velocities were observed in December–April. Velocities of DAW ($0.04 \pm 0.004 \text{ m s}^{-1}$) and AW ($0.04 \pm 0.004 \text{ m s}^{-1}$) were considerably weaker than BSBW and TAW (Figure 8a and Table 2) as these water masses occupied the off-shelf region where the boundary current was slowest ($<0.05 \text{ m s}^{-1}$) (Figures 4–6). Fluctuations in the area covered by BSBW were observed (Figure 8b), with maxima $>9 \text{ km}^2$ in April–October, which suggests a greater influence from this water mass of shelf origin into the Arctic Ocean during summer months. DAW covered an average area of 37 km^2 . The BSBW area evolution varied inversely to the area of DAW ($\gamma = -0.68$) and suggests that within the deep density layer basin-ward intrusions of BSBW led to retreats of DAW and vice-versa. Within the intermediate density layer, the average area covered by AW and TAW was 21 and 11 km^2 , respectively.

Transport of BSBW was on average $0.61 \pm 0.10 \text{ Sv}$ and varied with maximums between April and October–November ($>0.6 \text{ Sv}$) and minimums ($<0.5 \text{ Sv}$) between November–December and February–April

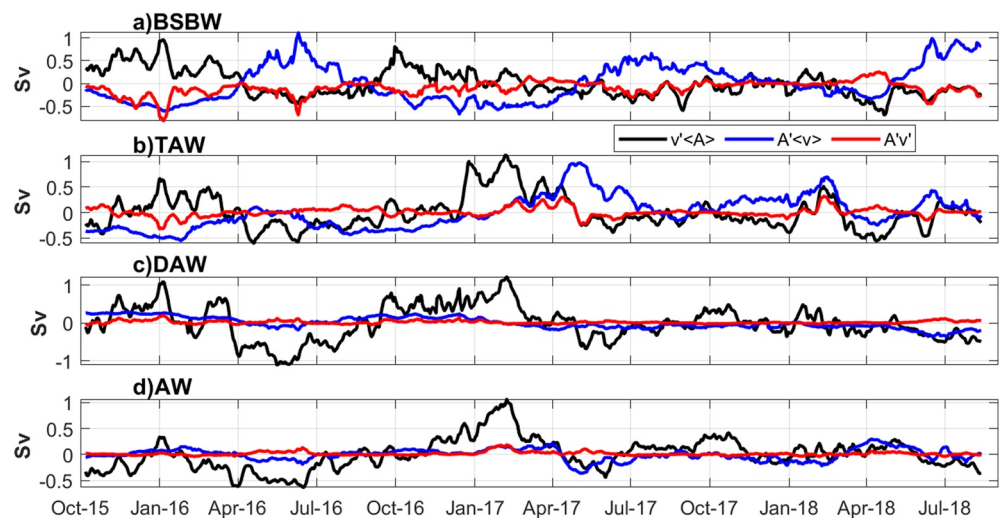


Figure 9. Transport decomposition for (a) Barents Sea Branch Water (BSBW), (b) Transformed Atlantic Water (TAW), (c) Dense Atlantic Water (DAW), and (d) AW. Black, blue, and red lines represent the velocity anomalies, area anomalies and the combinations of velocity and area anomalies.

(Table 2, Figure 8c). Transport variability was better correlated with variations in the area cover ($\gamma=0.76$) than with velocity oscillations which were insignificantly correlated ($\gamma<-0.03$), as maximum velocity anomalies were canceled out by minimum transport anomaly (Figure 9a). Transport of TAW was on average 1.0 ± 0.15 Sv (Table 2) and was maximum (>1.5 Sv) in October 2016 to May 2017 and January–March 2018 (Figure 8c). Area fluctuations and velocity had a comparable influence on transport variability (Figure 9b) which is consistent with similar correlation coefficients ($\gamma = 0.71$ – 0.72). Interestingly, between October 2015 and April 2016, transport of TAW was relatively low. Similarly to BSBW transport strong velocities were canceled out by minimums in the area cover (Figure 9b). DAW transport was 1.5 ± 0.19 Sv. Between October 2015 and April 2017 maximum and minimum transports occurred in September–March and April–July (Figure 8c). After April 2017 transports remained constant around (1.1 Sv). AW had an average transport of 0.88 ± 0.11 Sv with the strongest transport (>1.5 Sv) occurring between January and March 2017. For DAW and AW transports velocities had a greater effect than area as indicated by correlation coefficients of 0.95–0.96 and 0.64–0.68, respectively (Figures 9c and 9d). Total transport across the section in the depth range 50–1,000 m accounted for 4.15 ± 0.3 Sv.

The BSBW temperature time series was inversely correlated with transport variability ($\gamma = -0.6$) (Figures 8c and 8d). Temperature maximums (0.5°C) and minimums ($<0.2^{\circ}\text{C}$) were observed in November–May and June–October, respectively (Figure 8d), with an average temperature of $0.26 \pm 0.09^{\circ}\text{C}$ (Table 2). TAW had a mean temperature of $0.8 \pm 0.2^{\circ}\text{C}$ and showed the greatest variability with temperatures ranging between -0.1 and $\sim 1.6^{\circ}\text{C}$ with peaks in temperature between September–October and February and minimums in April–July. In contrast, throughout the record temperature of DAW and AW remained relatively constant at 0.64 ± 0.03 and $1.9 \pm 0.03^{\circ}\text{C}$. These water masses located further off the shelf edge showed the smallest variability.

3.3. Seasonality of the Water Masses in the ABC

The most striking summer-to-winter difference in the hydrography across the mooring array are the on-shelf and off-shelf intrusions and retreats of TAW and BSBW. In January, within the intermediate density layer TAW remained closer to the 300 m-isobath within 20 km between 150 and 300 m depth and distances around 10 km below 300 m (Figure 7c). Above the 300 m-isobath, temperatures reached values above 1°C . In contrast to winter conditions, TAW was observed up to 25–30 km between 150 and 450 m and maximum temperatures above the 300 m-isobath were below 0.5°C (Figure 7d). Further off the shelf slope, AW was located below ~ 180 m as determined by the location of the 35.06 g kg^{-1} isohaline in both January (Figure 7c) and June (Figure 7d). The maximum temperatures ($>2^{\circ}\text{C}$) of AW were found at depths shallower than 350 m in both months. Interestingly, the location of the salinity maximum was variable. In January, salinities above 35.11 g kg^{-1} were observed between 40 and 70 km and spanned from 200 to 800 m, while in June maximum salinities occurred further than

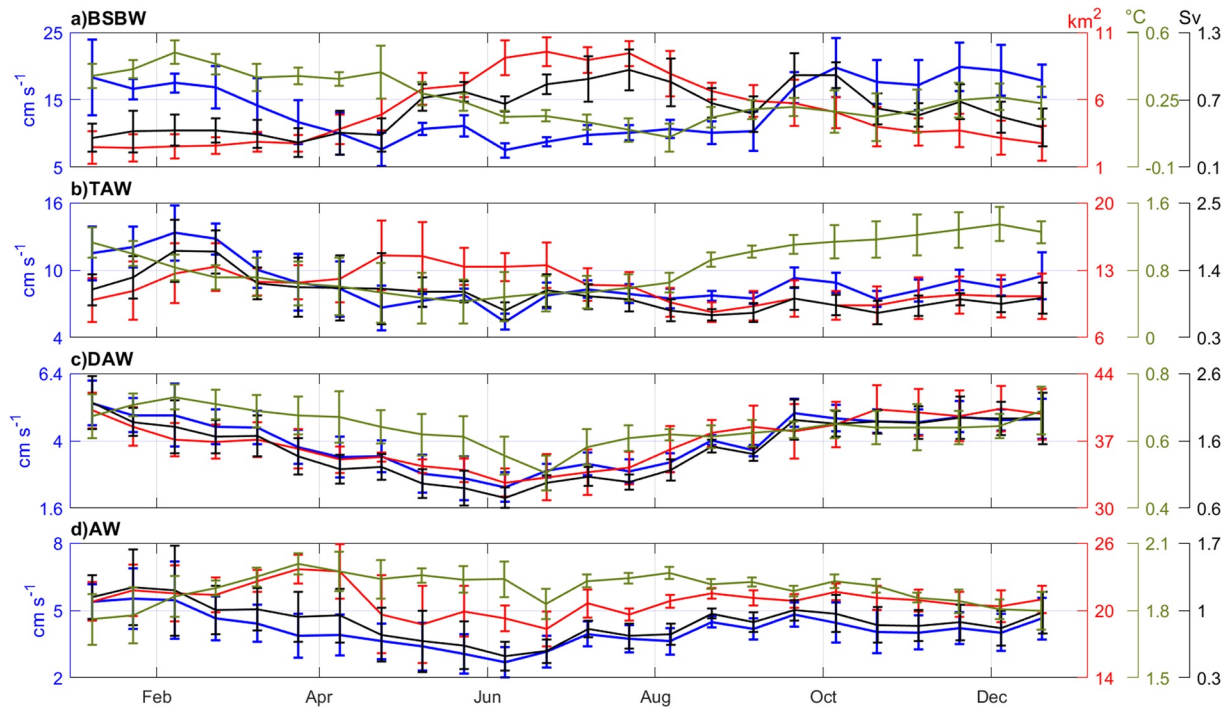


Figure 10. Seasonal variability of velocity (blue), area (red), temperature (green) and transport (black) for (a) Barents Sea Branch Water (BSBW), (b) Transformed Atlantic Water (TAW), (c) Dense Atlantic Water (DAW), and (d) AW. Error bars indicate the standard error.

50 km and were contained in the 200–400 m depth range. We speculate that these variations in the salinity maximum may arise from changes of the AW pathways between Fram Strait and Svalbard (Koenig et al., 2017). In the deep density layer, the off-shelf excursions, and retreats of BSBW were more notable. In January BSBW was constrained to a distance of 12 km, where temperatures ranged between 0 and 1°C. In contrast, in June BSBW showed temperatures below 0°C and the extension of this water mass reached distances beyond 20 km and seemed to force DAW to move poleward.

BSBW showed seasonal patterns in velocity, area coverage and transport that clearly differ from the other water masses (Figure 10). Interestingly, maximum transport (>0.7 Sv) in May–mid-October was first dominated by increases in area between May and August (Figure 10a). Afterward, the area coverage decreased while velocity increased and maintained transport above 0.7 Sv until mid-October. Nonetheless, transport fluctuations were only significantly correlated with area ($\gamma = 0.79$). For the remaining water masses, transport varied accordingly to changes in area and velocity (Figures 10b–10d). For transport of TAW, velocity ($\gamma = 0.79$) had a greater influence than area coverage ($\gamma = 0.54$) (Figure 10b). In contrast, transport of AW was better associated to velocity ($\gamma = 0.97$) than area variability ($\gamma = 0.68$) (Figure 10d). For DAW, variations in transport resembled fluctuations in velocity and area as indicated by correlation coefficients between 0.93 and 0.99 (Figure 10c). For AW, minima velocity (<0.023 m s⁻¹), area (<20 km²) and transport (<0.5 Sv) occurred between April and August (Figure 10d). However, the error bars on each of the parameters show seasonal variations in AW were minimum.

Fluctuations in temperature for BSBW and TAW were different from DAW and AW. Variability of BSBW temperature was mirrored by transport ($\gamma = -0.81$) (Figure 10a). Minimum temperature (<0.25°C) occurred between June and November and was the highest (0.5°C) between January and May when transport dropped to a minimum. Temperature variability was inversely linked to area cover ($\gamma = -0.74$). The temperature of TAW ranged between 0.4 and 1.3°C with minimums and maximums in March–August and September–January (Figure 10b) and was only significantly correlated with area ($\gamma = -0.75$). Contrary to the water masses located near the shelf break, oscillations in the temperature of DAW were positively correlated with transport, velocity and area ($\gamma = 0.89, \gamma = 0.85$ and $\gamma = 0.95$, respectively) (Figure 10c). Minimum temperatures (<0.6°C) coincided with minima in transport, velocity and area. For AW, error bars indicate that temperature remained relatively constant (Figure 10d).

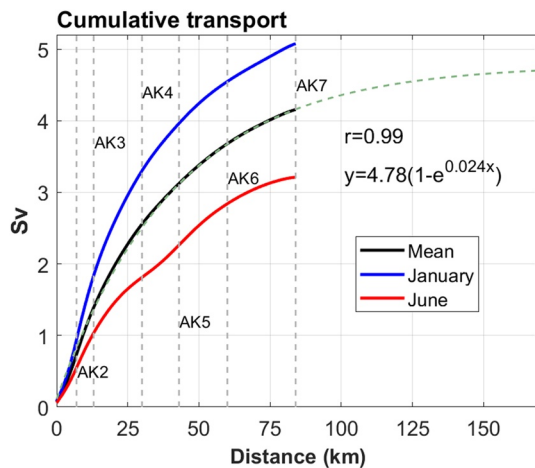


Figure 11. Measured cumulative transport along the mooring section for January (blue), June (red), and mean (black) and estimated cumulative transport (green). The gray dashed lines indicate the location of the moorings.

4. Discussion

4.1. Structure and Transport of the ABC

The three-year-velocity record was used to describe the spatial and seasonal variability of the ABC north of Severnaya Zemlya. Most of the variability of the ABC was constrained to 1-cpy fluctuations (Figures 6b and 6c). Current velocities of the ABC were greatest on the upper continental slope and gradually decreased northward into the deep basin (Figures 4–6). The vertical structure of the flow is largely baroclinic above the 300 m-isobath with maxima velocities between 100 and 220 m. There, the steeply upward sloping 27.97 kg m^{-3} isopycnal underlines the strong cross-slope density gradient between the waters of shelf origin and those advected from Fram Strait (Figures 5a, 7a and 7b). Farther away from the shelf break the average ABC flow was mainly barotropic. The highest EKE observed corresponded to the upper continental slope at the AK1–AK3 moorings (0–15 km of the transect) (Figure 5b). This agrees with previous Arctic Ocean studies, which reported an order of magnitude higher EKE along the continental slopes (depths > 1,000 m) than elsewhere (von Appen et al., 2022). North of AK3, the EKE in the ABC flow was weaker and indicates a relatively constant flow throughout the 3-year record (Figure 5b). The strongest and weakest velocities were observed in January and June, respectively (Figure 4, Figures 7a and 7b), with the ABC being almost twice as strong in January. The spatial flow patterns and their seasonality are similar to those previously observed within the ABC pathway at the continental slope northeast of Svalbard (30°E) (Pérez-Hernández et al., 2019) as well as in the northern Laptev Sea (125°E) (Baumann et al., 2018; Pnyushkov et al., 2018, 2021).

ities were observed in January and June, respectively (Figure 4, Figures 7a and 7b), with the ABC being almost twice as strong in January. The spatial flow patterns and their seasonality are similar to those previously observed within the ABC pathway at the continental slope northeast of Svalbard (30°E) (Pérez-Hernández et al., 2019) as well as in the northern Laptev Sea (125°E) (Baumann et al., 2018; Pnyushkov et al., 2018, 2021).

On average a total of $4.15 \pm 0.3 \text{ Sv}$ flowed across the region north of Severnaya Zemlya in the depth range 50–1,000 m where a total of 4 Sv accounted for AW, DAW, TAW, and BSBW. At Severnaya Zemlya most of the transport took place near the shelf break. The cumulative transport (Figure 11) indicates that 2.55 out of 4.15 Sv (62%) occurred within a distance of 30 km. At a 37 km-distance cumulative transport increased up to 2.9 Sv and accounted for 70%. Beyond 37 km increases in transport remained relatively low. In January and June, the cumulative transport was 5.1 and 3.2 Sv, respectively, where 73% and 63% of the total was found within a 37 km-distance. This underlines that the core of the ABC was constrained to within 30–40 km and is consistent with observations from northeast of Svalbard where the greatest velocities, that is, the core of the ABC, seemed to occur within $\sim 40 \text{ km}$ of the shelf slope (Pérez-Hernández et al., 2019). Interestingly, BSBW occupied the region where the core of the ABC was observed (Figures 5 and 7). Using the total transport at Severnaya Zemlya we can estimate the relative contribution of BSBW to the ABC. Throughout the record average transport of BSBW was 0.61 Sv (Figure 10 and Table 2) accounting for 24% of the ABC flow within 30 km of the shelf edge. Intrusion of BSBW has further implications on the volume transport of the ABC at Severnaya Zemlya. Observations from a 60 km-long across-slope transect northeast of Svalbard (30°E) indicate a transport of $3.97 \pm 0.32 \text{ Sv}$ between 100 and 1,200 m (Pérez-Hernández et al., 2019). Our estimates for an equally wide stretch north of Severnaya Zemlya found a cumulative transport of 3.7 Sv between 50 and 1,000 m. If we assume that the average velocity ($\sim 0.04 \text{ m s}^{-1}$) between 700 and 1,000 m represents the missing 9 km^2 ($150 \text{ m} \times 60 \text{ km}$) near the bottom, we get a volume transport of 0.36 Sv increasing the total transport to 4.06 Sv. Considering that this estimate contains 0.61 Sv of BSBW, which is not present in the boundary current northeast of Svalbard, our estimate of the non-BSBW related transport ($4.06 - 0.61 \approx 3.45 \text{ Sv}$) agrees reasonably well with the transport estimates of Pérez-Hernández et al. (2019). Downstream in the Laptev Sea, the ABC advects on average $4.8 \pm 0.1 \text{ Sv}$ in the top 800 m (Pnyushkov et al., 2021). However, a direct comparison between Severnaya Zemlya and Laptev Sea is difficult due to the broader distance that the measurements cover in the Laptev Sea.

We are aware that some along-slope transport may occur shoreward of the southernmost mooring (AK1). However, we expect the contribution in this region to be minimal as the water depth reduces to less than 150 m within 7 km south of mooring AK1, that is, integrated transport in the water column would remain relatively small despite of higher velocities. If we assume that the average velocity at AK1 is representative up to the 150 m-isobath, total cumulative transport between 50 and 150 m would account for 0.35 Sv. Yet, we expect the unobserved inshore transport to be significantly lower than this value, as observations from upstream off

the northeast Svalbard coast showed a sharp decrease in the velocities on the shelf away from the shelf break jet (Pérez-Hernández et al., 2019). We expect this to occur north of Severnaya Zemlya as well. Figure 11 also shows that the cumulative transport increases in the off-shelf direction (yet at a decreasing rate) all the way to AK7. This indicates that a certain fraction of the eastward flow of AW and DAW passed the array north of AK7 and could therefore not be observed. By fitting an exponential function, the estimate of the cumulative transport was extended into the interior Nansen Basin up to 170 km. From 160 km northward increases accounted for less than 0.003 Sv. Following this approximation, the unobserved transport north of AK7 amounts to 0.54 Sv and yields a total transport of 4.7 Sv.

A huge step in understanding the strength of the ABC was obtained by Spall (2013), using an ocean general circulation model with highly idealized geometry featuring only one (Fram Strait-like) Arctic-Subarctic gateway and simplistic boundary conditions. The author demonstrated that fresh water of shelf origin at the shelf break and saline Atlantic water deeper down found along the boundaries of the Arctic Ocean, result in opposing lateral salt fluxes between the boundary current and the Arctic Ocean interior. In the Arctic Ocean interior, a relatively weak vertical turbulent diffusion is then sufficient to maintain the halocline (and salt balance) and thereby the lateral density gradient that drives the boundary current. Our observations were taken in a particularly complex area of the ABC just downstream of the confluence of Fram Strait and Barents Sea-derived water masses. Given the presence of elevated levels of EKE on the inner part of the boundary current at the TAW–BSBW interface (Figure 5b), we expect the TAW to lose salt via diffusion to the BSBW branch inshore. Prominent interleaving structures between the two branches were previously shown to exist (e.g., Rudels et al., 2012). It would be intriguing to add to the Spall (2013) model setup a Barents Sea branch inflow to investigate its impact on the subtle balance of lateral and vertical salt fluxes required to sustain the boundary current.

4.2. Hydrographic Changes Along the ABC Pathway

The mean thermohaline characteristics varied significantly along the ABC pathway. Northeast of Svalbard the hydrographic properties are exclusively shaped by Atlantic Water. Temperatures and salinities between 100 and 700 m range from 1 to 4°C and 35–35.2 (or ~ 35.16 – 35.36 g kg⁻¹) (Pérez-Hernández et al., 2017) with yearlong averages of 1.5–2.4°C and 34.95–35.02 (or ~ 35.11 – 35.18 g kg⁻¹) (Pérez-Hernández et al., 2019), respectively. Interestingly, at Severnaya Zemlya, within 20 km of the 300-m isobath, temperature and salinity characteristics corresponded to TAW and BSBW (Figure 5c), which clearly indicates a change in the thermohaline properties along the ABC pathway. Averaged over the 2015–2018 period, temperature and salinity were below 1.5°C and 35.06 g kg⁻¹ with mean values of 0.8 ± 0.2 °C and 34.97 ± 0.006 g kg⁻¹ for TAW and 0.26 ± 0.09 °C and 35.04 ± 0.003 g kg⁻¹ for BSBW. Within the intermediate density layer the cooling and freshening of the ABC results from mixing with waters of shelf origin along the continental slope of the Barents Sea (Aksenov et al., 2011; Ivanov & Aksenov, 2013) and transforms AW into TAW. Furthermore, downstream, a fraction of the ABC's Fram Strait branch generally meanders into St. Anna Trough (Schauer et al., 2002). There, TAW mixes further with colder and fresher sub-surface water from the Barents Sea (Dmitrenko et al., 2014, 2015; Lien & Trofimov, 2013). TAW then exits on the eastern flank of St. Anna Trough and propagates eastward along the Eurasian Arctic continental slope to the Laptev Sea where hydrographic ABC characteristics similar to those observed in our mooring array had been reported previously (Baumann et al., 2018). In the deep density layer, most of the BSBW (>60%) joins the ABC through St. Anna Trough (Årthun et al., 2011). A smaller BSBW portion enters the ABC region across the shelf break west of Franz Josef Land (Schauer et al., 1997) as well as across the northern Kara Sea (Rudels et al., 2013). As the BSBW is denser than the DAW at the same depth (Figure 5c), an inflow of BSBW can effectively push the warmer DAW northward (Rudels et al., 2000) and cool and freshen the ABC by supplying colder and fresher waters (~ 0 – 0.5 °C and < 35.06 g kg⁻¹) to the continental slope. In 2015–2018 the BSBW was on average 1.0–1.5°C colder than temperatures found in the DAW residing in the same density range.

Contrary to the continental slope region, the AW located in the off-shelf part of the mooring transect (~ 40 km) appears to have only slightly cooled between the northern Barents Sea and Severnaya Zemlya. Average upstream temperatures were 2.0–2.5°C (Pérez-Hernández et al., 2017, 2019) and decreased to 1.9 ± 0.03 °C north of Severnaya Zemlya, while salinities remained between ~ 35.1 and 35.16 g kg⁻¹ (or 34.94 and 35.0) between both sites (Figure 5c and Table 2). These rather subtle hydrographic changes can be explained by the circulation patterns. Due to the distance between the outer ABC branch to the continental shelf, off-shelf waters cannot mix with colder and fresher waters from the Barents or Kara Seas and are further not affected by BSBW intrusions into the Arctic Ocean.

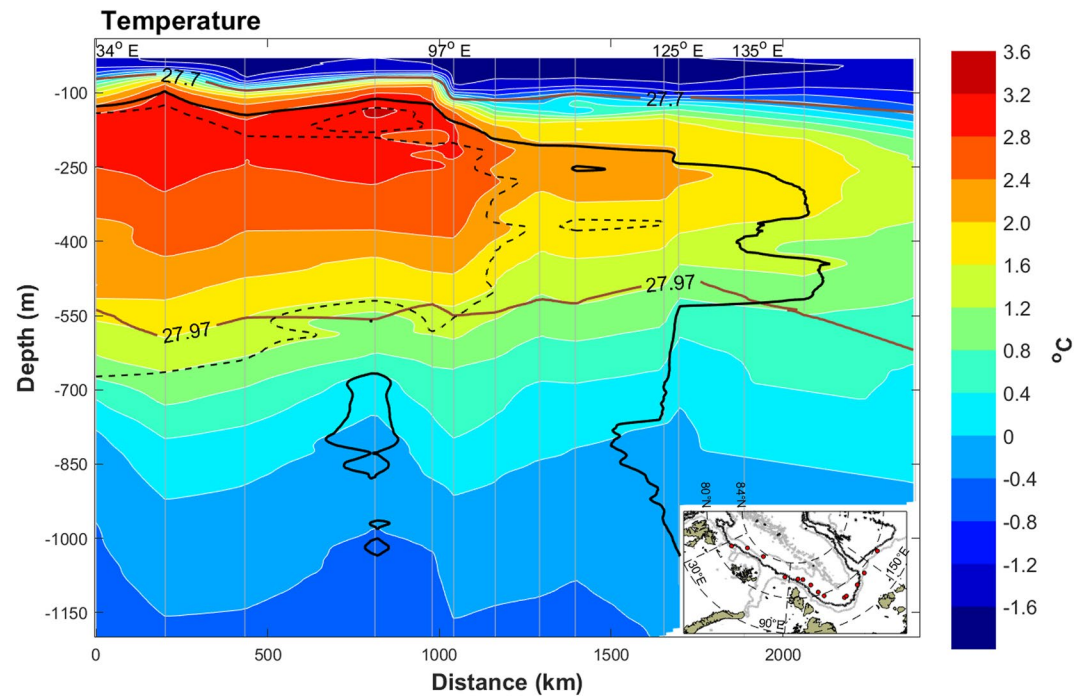


Figure 12. Along-slope section of Conservative Temperature (map in color), Absolute Salinity (black contours) and potential density (brown contours) from a “quasi-synoptic” Conductivity, Temperature, and Depth survey in summer 2007 (August–September). The thick and dashed contours indicate the 35.06 and 35.11 g kg^{-1} isohalines. In the small map red circles indicate the location of the casts. Each cast was obtained where temperature was maximum, that is, in the AW core. The gray and black contours represent the 3,500, 400, and 2,000 m isobaths, respectively.

In the deep basin transformation of AW occurs chiefly eastward of Severnaya Zemlya. Figure 12 shows a quasi-synoptic (August–September 2007) hydrographic section highlighting the location of the AW core along the eastern Arctic continental slope. The section was assembled from CTD data collected during different oceanographic cruises on board the research vessels Akademik Fedorov, Polarstern, and Victor Buinitsky. Consistent with our analysis, in the intermediate density layer, temperature and salinity remained relatively constant between northeast of Svalbard (34°E) and Severnaya Zemlya (97°E). In contrast, above 250 m between Severnaya Zemlya and the central Laptev Sea ($\sim 125\text{--}135^{\circ}\text{E}$), there was a simultaneous decrease in temperature and salinity from $2.8\text{--}3.2^{\circ}\text{C}$ to $-1.6\text{--}1.2^{\circ}\text{C}$ and from 35.11 g kg^{-1} to below 35.06 g kg^{-1} , respectively. To assess the degree of transformation we can estimate the relative contribution of the thickness of TAW to the intermediate density layer. At 34°E and 97°E the thickness of the density layer was $\sim 460\text{ m}$ of which TAW accounted for 12%, while in the central Laptev Sea, TAW represented 34%, or a 3-fold increase in the transformation of AW. Nonetheless, if we assume that velocities of $\sim 0.04\text{ m s}^{-1}$ (Figure 4) represent the mean velocity along the hydrographic transect, waters from Svalbard may take more than 2 years to reach the central Laptev Sea. It can be argued that the decrease in temperature east of Severnaya Zemlya may result from inter-annual variability in the temperature of AW entering through Fram Strait. However, it is less likely that the decrease in salinity between Severnaya Zemlya and the Laptev Sea was simultaneously influenced by inter-annual variability through Fram Strait, as for 2007, changes in salinity were not necessarily associated with changes in temperature (Richards et al., 2022). We attribute the decrease in temperature and salinity east of Severnaya Zemlya to transformation of AW. Interestingly, northeast of Svalbard and Severnaya Zemlya the warmest AW were observed between 100 and 250 m depth. East of Severnaya Zemlya the AW core deepened to 300 m depth at the central Laptev Sea.

4.3. Seasonality in Transformed Atlantic Water

The three year-long record north of Severnaya Zemlya enabled an assessment of the seasonality in ABC water mass transport. In the intermediate density layer, TAW showed a seasonality with maximum transports occurring between January and April (Figure 10b). Transports were similarly correlated with fluctuations in area and velocity (Figure 9b). AW showed no clear seasonal fluctuations in either transport, or area, or in velocity or

temperature (Figures 8 and 10d). At Severnaya Zemlya, the TAW temperature varied seasonally with highest and lowest temperatures occurring in October–February and April–July, respectively (Figure 10b). This seasonality cannot be attributed to encroachment of AW upon the continental shelf as temperature increases were not accompanied by on-shelf salinity intrusions (Figures 7c and 7d).

A simple estimation indicates that the seasonal variability in temperature is advected along the ABC pathway. Available mooring records on the eastern flank of St. Anna Trough between 2009 and 2010 indicate that maximum temperatures occur in July–December in the upper 140–200 m within the intermediate density layer (Dmitrenko et al., 2015). Between that mooring and our mooring array there is a ~400 km distance (from 81°N/73°E to 82°N/94°E). The mean TAW velocity observed at Severnaya Zemlya (Table 2) suggests that waters from the trough would reach Severnaya Zemlya within ~51 days. Therefore, the temperature maximum first observed in St. Anna Trough would be expected to occur at Severnaya Zemlya between September and March, which agrees with the seasonality found at the mooring site (Figure 10b). The seasonal variability in TAW results from the seasonal signal advected from Fram Strait (Bieszczynska-Moller et al., 2012; Ivanov et al., 2009; Ivanov & Repina, 2018; Schauer et al., 1997) combined with local seasonal cooling in the Barents Sea (Ingvaldsen & Loeng, 2009; Smedsrud et al., 2010) and along the ABC pathway (Duarte et al., 2020; Ivanov et al., 2016; Polyakov et al., 2011). A decrease in the rate of cooling in the Barents Sea and St. Anna Trough would result in advection of warmer waters along the continental slope within the intermediate density layer.

4.4. Seasonality in Barents Sea Branch Water

In the deep density layer, the three-year-record demonstrates that transport variability of BSBW was more closely linked to variations in area than in velocities (Figure 10a). For DAW transport, variability was mainly explained by velocity ($\gamma = 0.96$ – 0.99), compared to BSBW, which was mainly explained by variations in area ($\gamma = 0.76$ – 0.79). Nonetheless, the seasonal analysis revealed that despite a decrease in the area covered by BSBW, enhanced velocity maintained maximum transports between September and November (Figure 10a). The area of BSBW and DAW illustrate a signal that varied inversely (Figures 5d, 8b, 10a–10c) and showed relatively high correlation coefficients calculated from the long-term record ($\gamma = -0.68$) and seasonal analysis ($\gamma = -0.72$). This indicates that northward retreats of DAW were associated with BSBW export into the ABC (Rudels et al., 2013). During periods of relatively low transport, BSBW was constrained to within a 13-km distance (Figures 7c and 10a). Seasonal temperature fluctuations coincided with BSBW transport variability (Figure 10a). Both variables showed a significant negative correlation throughout the record ($\gamma = -0.59$) as well as in the seasonal analysis ($\gamma = -0.81$) which indicates that greater transport was associated with lower temperatures (Figure 10a). This agrees with modeling studies from the Barents Sea (Årthun et al., 2011) and with observations from St. Anna Trough (Dmitrenko et al., 2015), where enhanced BSBW outflow into the Arctic Ocean was attributed to denser water formation following increased heat loss. At Severnaya Zemlya, seasonality in BSBW transport derived from seasonal cooling in the Barents Sea where greater outflow was produced by enhanced cooling and BSBW formation.

Downstream of Severnaya Zemlya, hydrographic mooring records in 2013–2015 obtained along 125°E provided further evidence of the seasonal horizontal fluctuations of waters with BSBW and DAW characteristics ($M1_3$ in Figure 8 in Baumann et al., 2018). In July–September 2013 and 2015, temperature and salinity ranges corresponded to DAW properties along the 28.0 kg m^{-3} contour, that is, within the deep density layer, while the hydrography was similar to BSBW properties in December–February 2013–2014 and 2014–2015. This seasonality is opposite to Severnaya Zemlya where maximum BSBW transport and area were observed between June and November (Figure 10a) and might be explained by the translation time-period between both sites over an along-slope distance of ~1,000 km. If we assume that the BSBW characteristics observed in the Laptev Sea in December occurred in Severnaya Zemlya between June and November (1–6 months earlier) and consider a translation time of 3–4 months, we get an average velocity of 8.3–11.1 km day^{-1} . This velocity is only slightly lower than the mean velocity (12 km day^{-1}) observed in June–November north of Severnaya Zemlya (Figure 10a). This implies a slight reduction in the ABC's speed, which might be explained by the divergence of the isobaths along the continental slope. However, it is unclear whether the temperature and salinity signals associated with BSBW in the Laptev Sea were advected from Severnaya Zemlya or originated from the Kara and Laptev seas to join the ABC through Vilkitsky Trough (e.g., Aksenov et al., 2011; Bauch et al., 2016; Janout et al., 2017). Analogously to St. Anna Trough, the outflow of shelf waters through Vilkitsky Trough may likely disrupt the flow at the confluence of the swift and fresh Vilkitsky Strait outflow current (Janout et al., 2015) with the ABC.

5. Conclusions

The structure of the ABC and the seasonal variability in the region north of Severnaya Zemlya were assessed using a 2015–2018 mooring record of velocity and hydrography. The highest velocities occurred near the shelf edge where the flow showed a baroclinic structure. The velocities gradually decreased in the offshore direction, and farther from the shelf edge the flow was barotropic. Across the mooring section, velocities were two times higher in January than in June. Most of the ABC volume transport (62%–70%) took place within 30–40 km of the shelf edge. North of the observations, the increase in volume transport was relatively small and accounted for 13% (0.54 Sv) of the total volume transport estimated within the mooring array (0–84 km). The observed spatial and seasonal variability were coherent with previous studies along the ABC pathway on the continental slopes' northeast of Svalbard and in the Laptev Sea. Although the structure of the ABC was similar, at Severnaya Zemlya the hydrographic characteristics changed significantly within 20 km of the shelf edge. Along the Barents Sea shelf edge and in St. Anna Trough, AW from Fram Strait were transformed (i.e., cooled and freshened) into TAW. A seasonality was pronounced in the TAW, which is likely due to a combination of local shelf processes with seasonal signals advected from Fram Strait. Further off the shelf slope, in the deep basin Atlantic Water remained largely unmodified between Svalbard and Severnaya Zemlya, while east of Severnaya Zemlya, most of the transformation of Atlantic Water occurred. For BSBW, the seasonality originated from the Barents Sea with higher transport associated with lower temperatures and enhanced cooling in the shelf sea. In addition, BSBW joined the ABC mainly through St. Anna Trough and supplied cold and fresh waters into the ABC. Our analyses underline that the Barents Sea plays an important role in shaping water masses such as TAW and BSBW, which clearly affect the properties of the ABC in the Arctic Ocean. Observations made within the last decade indicate a transition toward warmer waters in the Barents Sea (Asbjørnsen et al., 2020; Levitus et al., 2009; Lind et al., 2018; Skagseth et al., 2008), which evidently leads to reductions in the Barents Sea's cooling effect on the ABC (Skagseth et al., 2020). If this trend continues, the ABC is likely to carry warmer waters into the eastern Arctic continental slope regions, which would further intensify the transition toward more Atlantic-typical conditions.

Data Availability Statement

The data of the Hydrographic and current data for the AK1-7 moorings can be found here: <https://doi.pangaea.de/10.1594/PANGAEA.951363>; <https://doi.pangaea.de/10.1594/PANGAEA.951394>; <https://doi.pangaea.de/10.1594/PANGAEA.954237>; <https://doi.pangaea.de/10.1594/PANGAEA.954244>; <https://doi.pangaea.de/10.1594/PANGAEA.954249>; <https://doi.pangaea.de/10.1594/PANGAEA.954299>; <https://doi.pangaea.de/10.1594/PANGAEA.954352>.

Acknowledgments

Eugenio Ruiz-Castillo was funded by the project CATS-Synthesis (Grant 03F0831B) granted by the German Ministry of Education and Research (BMBF). Additional funding came from the EU project PASSION (101003472). Vladimir Ivanov was partly funded by the RSF Grant 19-17-00110-P. The authors also gratefully acknowledge the funding by the Deutsche Forschungsgemeinschaft (DFG, German Research Foundation) through the Transregional Collaborative Research Centre TRR-172 "Arctic Amplification: Climate Relevant Atmospheric and SurfaCe Processes, and Feedback Mechanisms (AC)3" (Grant 268020496). The moorings representing the basis of the study were deployed during the NABOS expedition in 2015, and the authors acknowledge the strong support by Dr. Igor Polyakov at that time. The authors would like to thank the captains and crews of the vessel Akademik Tryoshnikov who were involved in both the deployment and the recovery of the moorings in the ice-covered areas north of the Arctic Cape in 2015 and 2018. Open Access funding enabled and organized by Projekt DEAL.

References

- Aagard, K., Foldvik, A., & Hillman, S. R. (1987). The west spitsbergen current: Disposition and water mass transformation. *Journal of Geophysical Research*, 92(C4), 3778–3784.
- Aksenov, Y., Ivanov, V. V., Nurser, A. J. G., Bacon, S., Polyakov, I. V., Coward, A. C., et al. (2011). The arctic circumpolar boundary current. *Journal of Geophysical Research*, 116, C09017. <https://doi.org/10.1029/2010JC006637>
- Årthun, M., Ingvaldsen, R. B., Smedsrud, L. H., & Schrum, C. (2011). Dense water formation and circulation in the Barents Sea. *Deep-Sea Research*, 58(8), 801–817. <https://doi.org/10.1016/j.dsr.2011.06.001>
- Asbjørnsen, H., Årthun, M., Skagseth, Ø., & Eldevik, T. (2020). Mechanisms underlying recent arctic atlantification. *Geophysical Research Letters*, 47(15), e2020GL088036. <https://doi.org/10.1029/2020GL088036>
- Bauch, D., Cherniavskaya, E., & Timokhov, L. (2016). Shelf basin exchange along the siberian continental margin: Modification of atlantic water and lower halocline water. *Deep-Sea Research*, 115, 188–198. <https://doi.org/10.1016/j.dsr.2016.06.008>
- Baumann, T. M., Polyakov, I. V., Pnyushkov, A. V., Rember, R., Ivanov, V. V., Alkire, M. B., et al. (2018). On the seasonal cycles observed at the continental slope of the eastern Eurasian basin of the Arctic Ocean. *Journal of Physical Oceanography*, 48(7), 1451–1470. <https://doi.org/10.1175/JPO-D-17-0163.1>
- Beszczynska-Möller, A., Fahrback, E., Schauer, U., & Hansen, E. (2012). Variability in Atlantic water temperature and transport at the entrance to the Arctic Ocean, 1997–2010. *ICES Journal of Marine Science*, 69. <https://doi.org/10.1093/icesjms/fss056>
- Bluhm, B. A., Janout, M. A., Danielson, S. L., Ellingsen, I., Gavrilov, M., Grebmeier, J. M., et al. (2020). The pan-arctic continental slope: Sharp gradients of physical processes affect pelagic and benthic ecosystems. *Frontiers in Marine Science*, 7, 544386. <https://doi.org/10.3389/fmars.2020.544386>
- Carmack, E., Polyakov, I., Padman, L., Fer, I., Hunke, E., Hutchings, J., et al. (2015). Toward quantifying the increasing role of oceanic heat in sea ice loss in the new arctic. *The Bulletin of the American Meteorological Society*, 96(12), 2079–2105. <https://doi.org/10.1175/BAMS-D-13-00177.1>
- Dmitrenko, I. A., Bauch, D., Kirillov, S. A., Koldunov, N., Minnet, P. J., Ivanov, V. V., et al. (2009). Barents sea upstream events impact the properties of atlantic water inflow into the Arctic Ocean: Evidence from 2005 to 2006 downstream observations. *Deep-Sea Research*, 1(56), 513–527. <https://doi.org/10.1016/j.dsr.2008.11.005>

- Dmitrenko, I. A., Kirillov, S. A., Serra, N., Koldunov, N. V., Ivanov, V. V., Schauer, U., et al. (2014). Heat loss from the atlantic water layer in the northern Kara Sea: Causes and consequences. *Ocean Science*, *10*, 719–730. <https://doi.org/10.5194/os-10-719-2014>
- Dmitrenko, I. A., Rudels, B., Kirillov, S. A., Aksenov, Y. O., Lien, V. S., Ivanov, V. V., et al. (2015). Atlantic water flow into the Arctic Ocean through the st. Anna trough in the northern Kara Sea. *Journal of Geophysical Research*, *120*, 5158–5178. <https://doi.org/10.1002/2015JC010804>
- Duarte, P., Sundfjord, A., Meyer, A., Hudson, S. R., Spreen, G., & Smedsrud, L. H. (2020). Warm atlantic water explains observed sea ice melt rates north of svalbard. *Journal of Geophysical Research*, *125*, e2019JC015662. <https://doi.org/10.1029/2019JC015662>
- Fer, I. (2009). Weak vertical diffusion allows maintenance of cold halocline in the central arctic. *Atmospheric Oceanographic Sciences Library*, *2*(3), 148–152. <https://doi.org/10.1080/16742834.2009.11446789>
- Gammelsrød, T., Leikvin, Ø., Lien, V., Budgett, W. P., Loeng, H., & Maslowski, W. (2009). Mass and heat transports in the NE Barents Sea: Observations and models. *Journal of Marine Systems*, *75*, 56–69. <https://doi.org/10.1016/j.jmarsys.2008.07.010>
- Ingvaldsen, R., & Loeng, H. (2009). *Ecosystem barents sea* (pp. 33–64). Tapir Academic Press Trondheim.
- Ivanov, V., Smirnov, A., Alexeev, V., Koldunov, N. V., Repina, I., & Semenov, V. (2018). Contribution of convection-induced heat flux to winter ice decay in the western Nansen Basin. *Journal of Geophysical Research*, *123*(9), 6581–6597. <https://doi.org/10.1029/2018JC013995>
- Ivanov, V. V., & Aksenov, E. O. (2013). Atlantic water transformation in the eastern Nansen Basin: Observations and modelling. *Problemy Arctiki*, *1*(95), 72–87.
- Ivanov, V. V., Alexeev, V., Koldunov, N. V., Repina, I., Sandø, A. B., Smedsrud, L. H., & Smirnov, A. (2016). Arctic Ocean heat impact on regional ice decay: A suggested positive feedback. *Journal of Physical Oceanography*, *46*(5), 1437–1456. <https://doi.org/10.1175/PO-D-15-0144.1>
- Ivanov, V. V., Alexeev, V. A., Repina, I., Koldunov, N. V., & Smirnov, A. (2012). Tracing atlantic water signature in the arctic sea ice cover east of svalbard. *Advances in Meteorology*, 1–11. <https://doi.org/10.1155/2012/201818>
- Ivanov, V. V., Polyakov, I. V., Dmitrenko, I. A., Hansen, E., Repina, I. A., Kirillov, S. A., et al. (2009). Seasonal variability in atlantic water off spitsbergen. *Deep-Sea Research*, *56*(1), 1–14. <https://doi.org/10.1016/j.dsr.2008.07.013>
- Ivanov, V. V., & Repina, I. A. (2018). The effect of seasonal variability of atlantic water on the arctic sea ice cover. *Izvestiya – Atmospheric and Oceanic Physics*, *54*, 65–72. <https://doi.org/10.1134/s0001433818010061>
- Jakobsson, M., Mayer, L. A., Bringensparr, C., Castro, C. F., Mohammad, R., Johnson, P., et al. (2020). The international bathymetric chart of the Arctic Ocean version 4.0. *Scientific Data*, *7*, 176. <https://doi.org/10.1038/s41597-020-0520-9>
- Janout, M., Aksenov, Y., Hölemann, J. A., Rabe, B., Schauer, U., Polyakov, I. V., et al. (2015). Kara Sea freshwater transport through vilkitsky strait: Variability, forcing, and further pathways toward the western Arctic Ocean from a model and observations. *Journal of Geophysical Research*, *120*, 4925–4944. <https://doi.org/10.1002/2014JC010635>
- Janout, M., Hölemann, J., Timokhov, L., Gutjahr, O., & Heinemann, G. (2017). Circulation in the northwest Laptev Sea in the eastern Arctic Ocean: Crossroads between siberian river water, atlantic water and polynya-formed dense water. *Journal of Geophysical Research*, *122*(8), 6630–6647. <https://doi.org/10.1002/2017JC013159>
- Jerónimo, G., & Gómez-Valdés, J. (2007). A subsurface warm-eddy off northern Baja California in July 2004. *Geophysical Research Letters*, *34*(6), L06610. <https://doi.org/10.1029/2006GL028851>
- Koenig, Z., Provost, C., Villacieros-Robineau, N., Sennéchaël, N., Meyer, A., Lellouche, J.-M., & Garric, G. (2017). Atlantic waters inflow north of Svalbard: Insights from IAOOS observations and Mercator Ocean global operational system during N-ICE2015. *Journal of Geophysical Research*, *122*, 1254–1273. <https://doi.org/10.1002/2016jc012424>
- Lenn, Y. D., Wiles, P. J., Torres-Valdes, S., Abrahamson, E. P., Rippeth, T. P., Simpson, J. H., et al. (2009). Vertical mixing at intermediate depths in the Arctic boundary current. *Geophysical Research Letters*, *36* (5), L05601. <https://doi.org/10.1029/2008GL036792>
- Le Traon, P. Y. (1990). A method for optimal analysis of fields with spatially variable mean. *Journal of Geophysical Research*, *95*, 13542–13543. <https://doi.org/10.1029/jc095ic08p13543>
- Levitus, S., Matishov, G., Seidov, D., & Smolyar, I. (2009). Barents sea multidecadal variability. *Geophysical Research Letters*, *36*(19), L19604. <https://doi.org/10.1029/2009GL039847>
- Lien, V. S., & Trofimov, A. G. (2013). Formation of Barents sea branch water in the north-eastern Barents sea. *Polar Research*, *32*(1), 18905. <https://doi.org/10.3402/polar.v32i0.18905>
- Lind, S., Ingvaldsen, R. B., & Furevik, T. (2016). Arctic layer salinity controls heat loss from deep Atlantic layer in seasonally ice-covered areas of the Barents sea. *Geophysical Research Letters*, *43*(10), 5233–5242. <https://doi.org/10.1002/2016GL068421>
- Lind, S., Ingvaldsen, R. B., & Furevik, T. (2018). Arctic warming hotspot in the northern Barents sea linked to declining sea-ice import. *Nature Climate Change*, *8*, 634–639. <https://doi.org/10.1038/s41558-018-0205-y>
- McDougall, T. J., & Barker, P. M. (2011). *Getting started with TEOS-10 and the gibbs seawater (GSW) oceanographic toolbox*. SCOR/IAPSO WG127.
- Nurser, A. J. G., & Bacon, S. (2014). The rossby radius in the Arctic Ocean. *Ocean Science*, *10*, 967–975. <https://doi.org/10.5194/os-10-967-2014>
- Pérez-Hernández, M. D., Pickart, R. S., Pavlov, V., Våge, K., Ingvaldsen, R., Sundfjord, A., et al. (2017). The Atlantic water boundary current north of Svalbard in late summer. *Journal of Geophysical Research*, *122*, 2269–2290.
- Pérez-Hernández, M. D., Pickart, R. S., Torres, D. J., Bahr, F., Sundfjord, A., Ingvaldsen, R., et al. (2019). Structure, transport, and seasonality of the atlantic water boundary current north of svalbard: Results from a yearlong mooring array. *Journal of Geophysical Research*, *124*(3), 1679–1698. <https://doi.org/10.1029/2018JC014759>
- Pnyushkov, A. V., Polyakov, I. V., Alekseev, G. V., Ashik, I. M., Baumann, T. M., Carmack, E. C., et al. (2021). A steady regime of volume and heat transports in the eastern Arctic Ocean in the early 21st century. *Frontiers in Marine Science*, *8*, 705608. <https://doi.org/10.3389/fmars.2021.705608>
- Pnyushkov, A. V., Polyakov, I. V., Ivanov, V. V., Aksenov, Y., Coward, A. C., Janout, M., & Rabe, B. (2015). Structure and variability of the boundary current in the Eurasian basin of the Arctic Ocean. *Deep-Sea Research*, *1*(101), 80–97. <https://doi.org/10.1016/j.dsr.2015.03.001>
- Pnyushkov, A. V., Polyakov, I. V., Rember, R., Ivanov, V. V., Alkire, M. B., Ashik, I. M., et al. (2018). *Ocean Science*, *14*, 1349–1371. <https://doi.org/10.5194/os-14-1349-2018>
- Polyakov, I. V., Alexeev, V. A., Ashik, I. M., Bacon, S., Beszczynska-Möller, A., Carmack, E. C., et al. (2011). Fate of early 2000s arctic warm water pulse. *The Bulletin of the American Meteorological Society*, *92*(5), 561–566. <https://doi.org/10.1175/2010BAMS2921.1>
- Polyakov, I. V., Pnyushkov, A. V., Alkire, M. B., Ashik, I. M., Baumann, T. M., Carmack, E. C., et al. (2017). Greater role for atlantic inflows on sea-ice loss in the Eurasian basin of the Arctic Ocean. *Science*, *356*, 285–291. <https://doi.org/10.1126/science.aai8204>
- Polyakov, I. V., Rippeth, T. P., Fer, I., Alkire, M. B., Baumann, T. M., Carmack, E. C., et al. (2013). Weakening of the cold halocline layer exposes sea ice to oceanic heat in the eastern Arctic Ocean. *Journal of Climate*, *33*, 8107–8123. <https://doi.org/10.1175/JCLI-D-19-0976.1>
- Polyakov, I. V., Rippeth, T. P., Fer, I., Baumann, T. M., Carmack, E. C., Ivanov, V. V., et al. (2020). Intensification of near-surface currents and shear in the eastern Arctic ocean. *Geophysical Research Letters*, *47*(16), e2020GL089469. <https://doi.org/10.1029/2020gl089469>

- Polyakov, I. V., Timokhov, L. A., Alexeev, V. A., Bacon, S., Dmitrenko, I. A., Fortier, L., et al. (2010). Arctic Ocean warming contributes to reduced polar ice cap. *Journal of Physical Oceanography*, *40*(12), 2743–2756. <https://doi.org/10.1175/2010JPO4339.1>
- Richards, A. E., Johnson, H. L., & Lique, C. (2022). Spatial and temporal variability of atlantic water in the arctic from 40 years of observations. *Journal of Geophysical Research*, *127*(9). <https://doi.org/10.1029/2021jc018358>
- Rudels, B. (2009). Arctic ocean circulation. In J. H. Steele, S. A. Thorpe, & K. K. Turekian (Eds.), *Encyclopedia of ocean sciences* (pp. 211–225). Academic Press. <https://doi.org/10.1016/B978-012374473-9.00601-9>
- Rudels, B., Anderson, L., Eriksson, P., Fahrbach, E., Jakobsson, M., Jones, E. P., et al. (2012). Observations in the ocean. In P. Lemke & H. Jacobi (Eds.), *Arctic climate change: The ACSYS decade and beyond, atmospheric and oceanographic sciences library 43*. Springer Science Business Media B.V. https://doi.org/10.1007/978-94-007-2027-5_4
- Rudels, B., Anderson, L. G., & Jones, E. P. (1996). Formation and evolution of the surface mixed layer and halocline of the Arctic Ocean. *Journal of Geophysical Research*, *110*(C4), 8807–8821. <https://doi.org/10.1029/96JC00143>
- Rudels, B., Björk, G., Nilsson, J., Winsor, P., Lake, I., & Nohr, C. (2005). The interaction between waters from the Arctic Ocean and the nordic seas north of Fram Strait and along the east greenland current: Results from the Arctic Ocean-02 oden expedition. *Journal of Marine Systems*, *55*, 1–30. <https://doi.org/10.1016/j.jmarsys.2004.06.008>
- Rudels, B., Jones, E. P., Schauer, U., & Eriksson, P. (2004). Atlantic sources of the Arctic Ocean surface and halocline waters. *Polar Research*, *23*(2), 181–208. <https://doi.org/10.3402/polar.v23i2.6278>
- Rudels, B., Muench, R. D., Gunn, J., Schauer, U., & Friedrich, H. J. (2000). Evolution of the Arctic Ocean boundary current north of the Siberian shelves. *Journal of Marine Systems*, *25*(1), 77–99. [https://doi.org/10.1016/S0924-7963\(00\)00009-9](https://doi.org/10.1016/S0924-7963(00)00009-9)
- Rudels, B., Schauer, U., Björk, G., Korhonen, M., Pisarev, S., Rabe, B., & Wisotzki, A. (2013). Observations of water masses and circulation with focus on the Eurasian Basin of the Arctic Ocean from the 1990s to the late 2000s. *Ocean Science*, *9*, 147–169. <https://doi.org/10.5194/os-9-147-2013>
- Schauer, U., Fahrbach, E., Osterhus, S., & Rohdard, G. (2004). Arctic warming through the Fram Strait: Oceanic heat transport from 3 years of measurements. *Journal of Geophysical Research*, *109*, C06026. <https://doi.org/10.1029/2003JC001823>
- Schauer, U., Loeng, H., Rudels, B., Ozhigin, V. K., & Dieck, W. (2002). Atlantic water flow through the Barents and Kara seas. *Deep-Sea Research*, *1*(49), 2281–2298. [https://doi.org/10.1016/s0967-0637\(02\)00125-5](https://doi.org/10.1016/s0967-0637(02)00125-5)
- Schauer, U., Muench, R. D., Rudels, B., & Timokhov, L. (1997). Impact of eastern Arctic shelf waters on the Nansen Basin intermediate layers. *Journal of Geophysical Research*, *102*(C2), 3371–3382. <https://doi.org/10.1029/96jc03366>
- Schulz, K., Janout, M., Lenn, Y.-D., Ruiz-Castillo, E., Polyakov, I., Mohrholz, V., et al. (2021). On the along-slope heat loss of the boundary current in the eastern Arctic Ocean. *Journal of Geophysical Research*, *126*, e2020JC016375. <https://doi.org/10.1029/2020JC016375>
- Shapiro, G. I., Huthnance, J. M., & Ivanov, V. V. (2003). Dense water cascading off the continental shelf. *Journal of Geophysical Research*, *108*, 3390. <https://doi.org/10.1029/2002JC001610>
- Skagseth, Ø., Eldevik, T., Årthun, M., Asbjørnsen, H., Lien, V. S., & Smedsrud, L. H. (2020). Reduced efficiency of the Barents Sea cooling machine. *Nature Climate Change*, *10*, 661–666. <https://doi.org/10.1038/s41558-020-0772-6>
- Skagseth, Ø., Furevik, T., Ingvaldsen, R., Loeng, H., Mork, K. A., Orvik, K. A., & Ozhigin, V. (2008). Volume and heat transports to the Arctic Ocean via the Norwegian and Barents seas. In R. R. Dickson, J. Meincke, & P. Rhines (Eds.), *Arctic-subarctic ocean fluxes*. Springer. https://doi.org/10.1007/978-1-4020-6774-7_3
- Smedsrud, L. H., Ingvaldsen, R., Nilsen, J. E. Ø., & Skagseth, Ø. (2010). Heat in the Barents Sea: Transport, storage, and surface fluxes. *Ocean Science*, *6*, 219–234. <https://doi.org/10.5194/os-6-219-2010>
- Spall, M. A. (2013). On the circulation of atlantic water in the Arctic Ocean. *Journal of Physical Oceanography*, *43*(11), 2352–2371. <https://doi.org/10.1175/jpo-d-13-079.1>
- Von Appen, W.-J., Baumann, T., Janout, M., Koldunov, N., Lenn, Y.-D., Pckart, R. S., et al. (2022). Eddies and the distribution of eddy kinetic energy in the Arctic Ocean. *Oceanography*. Special issue “The Changing Arctic Ocean”. <https://doi.org/10.5670/oceanog.2022.122>
- Von Appen, W.-J., Lochthofen, N., Nöthig, E.-M., & Schewe, I. (2019). Physical oceanography and current meter data from mooring F4-S-2. *PANGAEA*. <https://doi.org/10.1594/PANGAEA.904472>
- Woodgate, R., Aagaard, K., Muench, R. D., Gunn, J., Björk, G., Rudels, B., et al. (2001). The Arctic Ocean boundary current along the Eurasian slope and the adjacent Lomonosov Ridge: Water mass properties, transports and transformations from moored instruments. *Deep Sea Research Part 1*, *48*(18), 1757–1792. [https://doi.org/10.1016/S0967-0637\(00\)00091-1](https://doi.org/10.1016/S0967-0637(00)00091-1)